Quaternary Science Reviews 375 (2026) 109753

Contents lists available at ScienceDirect

Quaternary Science Reviews

journal homepage: www.elsevier.com/locate/quascirev

Holocene climatic changes in the Kerguelen archipelago (South Indian Ocean) based on marine and lacustrine palaeoclimatic archives

Emeline Bellet [a,*], Guillemette Ménot [b], Christine Piot [a], Xavier Crosta [c], Vincent Grossi [b,d], Marie-Alexandrine Sicre [e], Mercedes Mendez-Millan [e], Vincent Klein [e], Salomé Ansanay-Alex [b], Matthew Makou [b], Jérôme Poulenard [a], Emmanuel Malet [a], Bernard Fanget [a], Eivind Støren [f], Nicolas Leviavan [g], Aymeric Servettaz [h], Jostein Bakke [f], Pierre Sabatier [a], Fabien Arnaud [a]

[a] EDYTEM, Université Savoie Mont-Blanc, CNRS, Chambéry, France
[b] ENS Lyon, UCBL, CNRS, UMR 5276, LGL-TPE, Lyon, France
[c] EPOC, Université de Bordeaux, CNRS, Bordeaux INP, Bordeaux, France
[d] MIO, Aix-Marseille Université, Université de Toulon, CNRS, IRD Marseille, France
[e] LOCEAN, IPSL, Sorbonne Université, CNRS, IRD, MNHN, Paris, France
[f] Department of Earth Science and Bjerknes Centre for Climate Research, University of Bergen, Bergen, Norway
[g] Institut Polaire, Paul-Emile Victor, Plouzané, France
[h] Institute of Arctic Climate and Environment Research, Japan Agency for Marine–Earth Science and Technology, Kanagawa, Japan

ARTICLE INFO

Handling Editor: P Rioual

ABSTRACT

Climatic variability in the Southern Hemisphere is largely controlled by the latitudinal position of the Southern Hemisphere Westerly Winds (SHW), whose migration influences precipitation, temperature, and Antarctic upwelling. This study presents the results of analyses of two lacustrine sediment cores from Lake Armor, located on the subantarctic Kerguelen Islands (49°15′S, 69°10′E), within the SHW belt. Lipid biomarkers (Glycerol Dialkyl Glycerol Tetraethers, *n*-alkanes, and their hydrogen isotopes) were used to reconstruct mean annual air temperature above freezing (MAF) and humidity conditions. These records are compared with a high-resolution diatom-based summer sea surface temperature (SST) reconstruction from marine core MD11-3353, situated 150 km southwest of Lake Armor.

In the late glacial and Early Holocene, our results reveal a period of warm air temperature, comparable to current values and very warm sea surface temperature, 5 °C above the current values. Around 9000 cal a BP, an abrupt transition occurred, marked by a cooling of 5 °C in SST and 1.5 °C in MAF, interpreted as a northward migration of the SHW and associated oceanic fronts. The Mid-to-Late Holocene period is characterized by pronounced MAF variability, including a notably warm interval between 3000 and 2000 cal a BP, when *n*-alkane dD suggests the prevalence of wetter conditions. Since ~250 cal a BP, a southward migration of the SHW has produced a 2.5 °C rise in MAF.

Our findings are overall consistent with previous studies from the Indian Ocean, but permit us to go a step further as by comparing SSTs and air temperatures. This suggests that SST is not a reliable predictor of air temperature on the Kerguelen Islands, particularly during the Early Holocene. We hence argue that Kerguelen air temperature is predominantly controlled by the position of westerly winds, as an indicator of reorganisations in air mass trajectories.

1. Introduction

Palaeoclimate studies provide insights into the centennial-to millennial-scale natural variability that has modulated the Holocene and current climate change (Forster et al., 2020; Knutti et al., 2017). In the Southern Hemisphere, data remain sparse compared with those in the Northern Hemisphere (Erb et al., 2022), leading to a significant lack of knowledge. Among the main drivers of climate variability in the

* Corresponding author.
E-mail address: emeline.bellet@univ-smb.fr (E. Bellet).

https://doi.org/10.1016/j.quascirev.2025.109753
Received 2 June 2025; Received in revised form 10 December 2025; Accepted 11 December 2025
Available online 12 January 2026

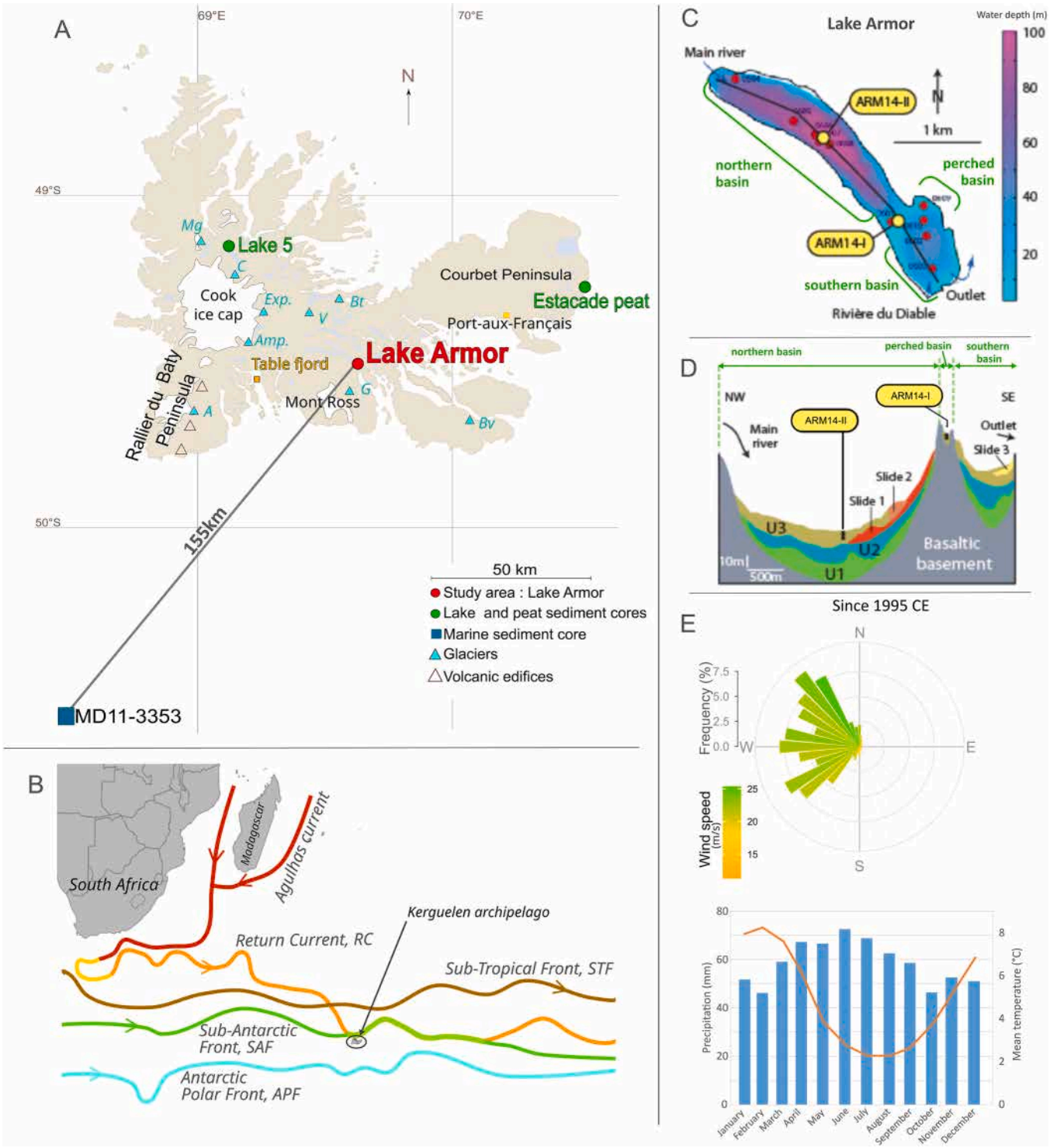

Fig. 1. Study Area. **A:** The main Island of the Kerguelen archipelago with the location of the principal features. Sediment cores: Lake 5 (Zwier et al., 2024),Estacade peat (Van der Putten et al., 2015), Table Fjord (Chassiot et al., 2024), MD11-3353 (Civel-Mazens et al., 2021a, 2021b, this study), Lake Armor (this study). Glaciers: Mg: Guynemer, Exp.:Explorateur, Bt: Bontemps, V: Val Travers, Amp.: Ampère, A: Arago, G: Gentil, Bv: Belvedere. **B:** Maps of the main oceanic currents around Kerguelen (Civel-Mazens et al., 2021b). Return current (RC), Sub-Tropical Front (STF), Sub-Antarctic Front (SAF), Antarctic Polar Front (APF). **C and D:** Lake sediment core locations along with Lake Armor bathymetry map and a simplified seismic profile, based on Heirman et al. (2012) and Arnaud et al. (2020). Sedimentary units (U1, U2 and U3) and slides were described in Heirman et al. (2012). **E:** Monthly mean meteorological data since 1995 CE, recorded at the French weather station at Port-aux-Français.

Southern Hemisphere, the strength and latitudinal position of the Southern Hemisphere Westerly Winds (SHW) are crucial parameters (Abram et al., 2014). These winds indeed influence regional climate patterns and govern the Antarctic Circumpolar Current (ACC) (Li et al., 2020; Moreno et al., 2018; Paterne et al., 2019; Toggweiler, 2009). The ACC is composed of different fronts: the Southern ACC Front (SACCF), the Antarctic Polar Front (APF) and the Sub-Antarctic Front (SAF) (Orsi et al., 1995; Rintoul et al., 2001; Sokolov and Rintoul, 2009). Their

position depends on the SHW position (Allison et al., 2010). Consequently, SHW shifts play a key role in the upwelling around Antarctica and, therefore, in the carbon pump (Moreno et al., 2010; Saunders et al., 2018; Toggweiler et al., 2006). Currently, during the austral summer, the SHW is strengthened and concentrated close to the Antarctic (Marshall, 2003, 2007). Indeed, over the last few decades, a large southward migration of the SHW belt has been observed in response to atmospheric warming induced by the increase in anthropogenic greenhouse gas emissions and ozone depletion (Gillett and Fyfe, 2013; Swart et al., 2015). This southward migration led to warm conditions and glacier retreats over the Southern Hemisphere (Favier et al., 2016a; Verfaillie et al., 2022), with potential impacts on the carbon pump (Saunders et al., 2018). However, observations are too short in time, and it is necessary to acquire palaeoclimate records to better understand these relationships over longer periods (Saunders et al., 2012).

Until recently, SHW's past dynamics research focused mainly on the Atlantic and Pacific sectors of the Southern Ocean (Foster et al., 2016; Gilli et al., 2005; Lamy et al., 2001, 2010; Moreno et al., 2018; Razik et al., 2013; Saunders et al., 2012, 2018; van der Bilt et al., 2022; Van Der Putten et al., 2004; Xia et al., 2020). In contrast, the Indian Ocean is sometimes referred to as the 'forgotten ocean', since little is known about the palaeoclimate evolution in this region, which is even more pronounced for the Southern Indian Ocean.

In the sub-Antarctic Indian Ocean, only a few studies have documented the relative position of SHW during the Holocene on the Kerguelen, Marion, Crozet and Amsterdam Islands (Van Der Putten et al., 2008; Van der Putten et al., 2015; Li et al., 2020; Perren et al., 2020; Charton et al., 2022; Chassiot et al., 2024; Zwier et al., 2024). These islands are key locations for climate reconstruction because of their geographic position and the potential of the continental archives to provide high-resolution palaeoclimate reconstructions (Van Der Putten et al., 2012). The Kerguelen Archipelago, in particular, currently lies in a strategic position, right on the Subantarctic water mass front and at the centre of the SHW belt (Fig. 1). However, tracking SHW past locations is challenging because of the absence of direct proxies (Spoth et al., 2023; Zwier et al., 2024). These studies are based on their interpretation of the observations of Fogt and Marshall (2020a) and Favier et al. (2016b), whereby shifts in the position of the SHW are accompanied by changes in air temperature and precipitation. When air temperature reconstructions are not available, some studies based their interpretations on sea surface temperatures (SST) (Jomelli et al., 2017, 2021; Charton et al., 2021, 2022; Tuestad et al., 2024b). Nevertheless, the air temperature can vary independently of the SST. On Kerguelen Island, only relative air temperature (colder/warmer) reconstructions based on glacier advances/retreats and palaeoecology data are available (Charton et al., 2021, 2022; Chassiot et al., 2024; Frenot et al., 1997; Jomelli et al., 2017, 2021; Tuestad et al., 2024; Van der Putten et al., 2015; Young and Schofield, 1973; Zwier et al., 2024). Glacier fluctuations are reconstructed from the presence of geomorphological remains such as preserved moraines (Charton et al., 2021, 2022; Jomelli et al., 2017, 2018; Sleire et al., 2025; Tuestad et al., 2024). However, glacier fluctuations depend not only on temperature but also on precipitation. Conversely, palaeoecological studies based on individual species found in lake or peat sedimentary archives (Van der Putten et al., 2015; Young and Schofield, 1973; Zwier et al., 2024) provide continuous, but qualitative, reconstructions. Therefore, a continuous and quantitative record of air temperature in Kerguelen Archipelago is still missing for the Holocene period in order to better understand the regional climate dynamics and the atmosphere-ocean coupling. Moreover, interpretations based on marine or atmospheric temperatures alone can be biased by oceanic current changes, which could be partially independent of SHW behaviour (Kim et al., 2012). Therefore, a multi-archive analysis addressing both atmospheric and marine temperatures is necessary to understand the complexity of the system. In this work, we aimed at investigating the position and strength of the SHW throughout the Holocene in the Southern Indian Ocean by comparing independent air and sea surface temperature reconstructions. SST were estimated from a diatom-based transfer function in core MD11-3353, taken 150 km to the southwest of Kerguelen Islands. Air temperature was reconstructed from lipid biomarkers (Glycerol Dialkyl Glycerol Tetraether lipids, GDGT) preserved in two sediment cores from Lake Armor on Kerguelen mainland. In addition, we propose an indirect reconstruction of precipitation and/or wind stress based on the hydrogen isotopic compositions of the *n*-alkanes preserved in the lake cores.

2. Materials and methods

2.1. Study area

In the south Indian Ocean, the Kerguelen-Gaussberg Oceanic Plateau forms a significant obstacle to the Antarctic Circumpolar Current (ACC), generating a division of the oceanic water masses (Park et al., 2009). Hence, the Subantarctic Front (SAF) passes to the north of Kerguelen, while the Antarctic Polar Front (APF) passes to its south. Further south, the Southern Antarctic Circumpolar Current Front (SACCF) follows the bathymetry through the Fawn Trough (Civel-Mazens et al., 2021a; Park et al., 2019). The latitudinal migration of APF-induced changes in productivity due to the remobilisation of iron from the sediments (Kim et al., 2009).

Kerguelen's main island has an area of 7215 km^2 (Fig. 1A). It is the emerged part of the Kerguelen-Gaussberg Oceanic Plateau. The west side is mountainous, whereas the topography of the east side is gentler, characterised by stratified basalt, incised by moderately deep valleys. The island has a cold oceanic climate, with little seasonal variations (Van der Putten et al., 2015) (Fig. 1E).

A weather station has been operated by Météo-France at Port-aux-Français on the east side of the island since 1950 CE. For the period 1995 to 2022, the mean annual air temperature was 5.0 °C, with an annual amplitude of 6 °C, and the mean annual precipitation was 703.5 mm at Port-aux-Français, with an annual amplitude of 26.5 mm (Fig. 1E). The latter value, which is rather low for a sub-Antarctic island, is due to a strong orogenic effect concentrating precipitations on the western side of the island, where the mean annual precipitation can reach 3200 mm (Frenot et al., 2001). The mean annual wind velocity was 9.7 m s^{-1}, and the wind direction was predominantly from the west (Fig. 1E).

2.2. Marine sediment core: MD11-3353

2.2.1. The core

The marine core MD11-3353 (50°34.02′S–68°23.13′E, 1568 m water depth) was collected onboard the R/V Marion Dufresne II in 2011 during the oceanographic expedition MD185 INDIEN-SUD 1. We selected this core due to its proximity to the Kerguelen Archipelago (155 km southwestward; Fig. 1A) and the previously established low-resolution Holocene SST reconstruction (Civel-Mazens et al., 2021a). The core is 38.50 m long and is composed of diatom oozes, of which the upper 1.90 m correspond to the Holocene period (Mazaud and Michel, 2011). At this location, the nearest oceanic front is currently the APF (Park et al., 2019). The modern summer SST at the core location is approximately 4.5 °C.

2.2.2. Dating and age model

The age model of core MD11-3353 was developed by correlating the TEX_L^{86} and radiolarian-based SST records to the EPICA Dome C δD record (Civel-Mazens et al., 2021b; Thöle et al., 2019). The age model of the upper part of the core was improved by the addition of 16 radiocarbon dates obtained from monospecific foraminifera *Neogloboquadrina pachyderma* sinistral (NPs) samples. The samples were prepared following standard protocols at the LMC14 Laboratory (Dumoulin et al., 2017) and the analyses were performed at the ARTEMIS AMS facility of the LMC14 National Laboratory (Moreau et al., 2020). The conventional ^{14}C dates were calibrated through a Bayesian model via the package

Table 1
Results of dated samples for core MD11-3353, with the radiocarbon ages and their error, the variable regional deviation of the reservoir age and its error, the age range (minimum and maximum) calculated by the Bayesian model in rbacon.

Core	Samples	Depth (m)	Conventional age (a BP)	Reservoir age (yr)	Calibrated ages (cal a BP) [min-max]
MD11-3353	SaCA 70219	1	1700 ± 30	400 ± 100	190–1270
MD11-3353	SaCA 51437	11	1885 ± 30	400 ± 100	370–1410
MD11-3353	SaCA 70220	21	2320 ± 30	400 ± 100	730–1940
MD11-3353	SaCA 51438	31	2510 ± 30	400 ± 100	930–2170
MD11-3353	SaCA 70221	41	3025 ± 30	400 ± 100	1470–2790
MD11-3353	SaCA 70222	51	5300 ± 30	400 ± 100	4290–5640
MD11-3353	SaCA 70223	61	5880 ± 30	400 ± 100	5010–6280
MD11-3353	SaCA 70224	71	6650 ± 30	400 ± 100	5890–7150
MD11-3353	SaCA 70225	81	7045 ± 30	400 ± 100	6290–7510
MD11-3353	SaCA 70226	91	7470 ± 30	400 ± 100	6760–7920
MD11-3353	SaCA 70227	101	8060 ± 30	400 ± 100	7400–8520
MD11-3353	SaCA 70229	121	8535 ± 30	400 ± 100	7850–9180
MD11-3353	SaCA 70231	141	9145 ± 35	400 ± 100	8480–9920
MD11-3353	SaCA 51439	151	10880 ± 40	400 ± 100	10730–12470
MD11-3353	SaCA 70232	171	12605 ± 40	500 ± 100	12820–14120
MD11-3353	SaCA 70233	191	12660 ± 45	500 ± 100	12870–14240

rbacon (version 3.2.0, Blaauw and Christen, 2011) developed for the R-platform, the Marine20 calibration (Heaton et al., 2020), and a variable marine reservoir deviation (ΔR) accounting for the outgassing of old carbon during the last part of the deglaciation (Table 1) (Gottschalk et al., 2020; Siani et al., 2013). Rbacon models were run with 8,800,000 iterations using the default options (Fig. 2). More information is presented in section 3.2.1.

2.2.3. Diatom analysis and transfer function

Sixty samples over the 0–190 cm section were analysed and combined with previously published data (Civel-Mazens et al., 2021a, 2021b) to obtain a 2–4 cm resolution. Sediment processing and slide preparation followed the methodology detailed in Crosta et al. (2020). Diatom counting was conducted as described in Crosta and Koç (2007). Approximately 350 diatom valves were counted in each sample at 1000 × magnification on a Nikon Eclipse 80i phase contrast microscope.

Summer (January to March) SST was estimated by applying the Modern Analog Technique (MAT) to fossil diatom assemblages. The modern database is composed of 257 surface sediment samples, called analogues, for which locations of modern summer SST were interpolated on a 1° × 1° grid from the World Ocean Atlas (Locarnini et al., 2018) through Ocean Data View (Schlitzer, 2002). The MAT was implemented from the "bioindic" package (Guiot and de Vernal, 2011) developed for the R-platform. For each fossil sample, we used the relative abundances of 33 species and the chord distance to select the 5 most similar analogues. The threshold above which the selected analogues are too dissimilar to the fossil assemblage is fixed at the first quartile of random distances on the validation modern dataset. The quantitative estimates of summer SST represent a distance-weighted average of the climate values associated with the selected and reliable modern analogues. This method yields an R^2 of 0.96 and a root mean square error or prediction (RMSEP) of 1.06 °C.

2.3. Continental sediment cores: Lake Armor

2.3.1. The cores

Kerguelen mainland hosts hundreds of lakes, ranging from small ponds to several kilometres-long lakes. Lake Armor (49.46°S-69.71°E) is located in the eastern part of the island (Fig. 1A–C), it is 4 km long and 500 m wide. While it is a fjord-type lake, Lake Armor's watershed is located about 40 km east of Mount Cook's ice-cap and does not currently receive any glacier meltwater. Seismic investigations suggested this disconnection occurred during the last deglaciation or even earlier (Heirman et al., 2012). Although the lake's water level is only a few metres above the current sea level, there is no evidence of seawater intrusion. In 2006, during the first mission of the PEISACG program, funded by the French polar institute (IPEV), bathymetry surveys revealed that the Armor Basin was composed of three sub-basins with different depths: the northern basin (100 m depth), the perched basin (20 m depth) and the southern basin (50 m depth) (Fig. 1C and D, Heirman et al., 2012). The lake sediments present three sediment units (Fig. 1D–Heirman et al., 2012). No temperature data are available for Lake Armor. A single measurement of the surface water temperature (4 °C) was taken during a fieldtrip in summer, when the mean air temperature was around 8 °C. This difference between air and water temperatures suggests an efficient mixing of the water column as denser waters reach the surface. This mixing is probably linked to persistent windy conditions all around the year. During the winter season, the absence of ice cover and windier conditions (mean air temperature of 2.5 °C as shown in Fig. 1E) should also favour mixing of the lake waters, precluding any inverse stratification. However, it is possible that the lake was stratified in the past under less windy and/or warmer summer conditions. Currently, the northern basin is fed by terrigenous input from the Northern River, whereas the perched basin is isolated and fed mainly by atmospheric and autochthonous inputs. Sediment cores were collected in 2014 at two separate sites in Lake Armor during a second expedition, PALAS1. One site is situated in the northern basin (Sites II, ARM14-II), while the other is positioned in the perched basin (Site I, ARM14-I). Both cores cover most of Unit 3 (U3; Fig. 1D), which was deposited when the glacier had completely retreated from the Lake Armor basin (Heirman et al., 2012). The vegetation around is predominantly composed of *Accaena magellanica, Azorella selago* and Poaceae, and no ligneous species are present. No important change in vegetation composition occurred on Kerguelen mainland during the Mid- and Late Holocene (Zwier et al., 2024). Therefore, our *n*-alkane hydrogen isotope reconstruction was not influenced by vegetation changes.

2.3.2. Dating and age model

Twelve and fourteen plant macrofossils were sampled in ARM14-I and ARM14-II, respectively, for AMS radiocarbon dating. Radiocarbon content was measured at the Laboratoire de Mesure 14C (LMC14) ARTEMIS at the CEA (Atomic Energy Commission) Institute at Saclay (samples referenced with the prefix Sac in Table 2) and at the Poznan Radiocarbon Laboratory (samples referenced with the prefix Poz in Table 2). Macroremains of terrestrial plants were picked for ^{14}C dating, except in the core ARM14-I, which did not contain any and for which radiocarbon dating was done on fragments of aquatic plants. However, as there is no carbonate in the catchment area, we do not expect any significant reservoir effect. Radiocarbon ages were calibrated using the SHcal20 calibration curve (Hogg et al., 2020). Then, we used a Bayesian model with the package rbacon (version 3.2.0), the R-based algorithm developed by Blaauw and Christen (2011), to generate an age/depth model. Two age models based on independent carbon ages were therefore computed for the two lacustrine lake cores. Ages are expressed in calibrated years *Before Present* (cal a BP), being before 1950 CE.

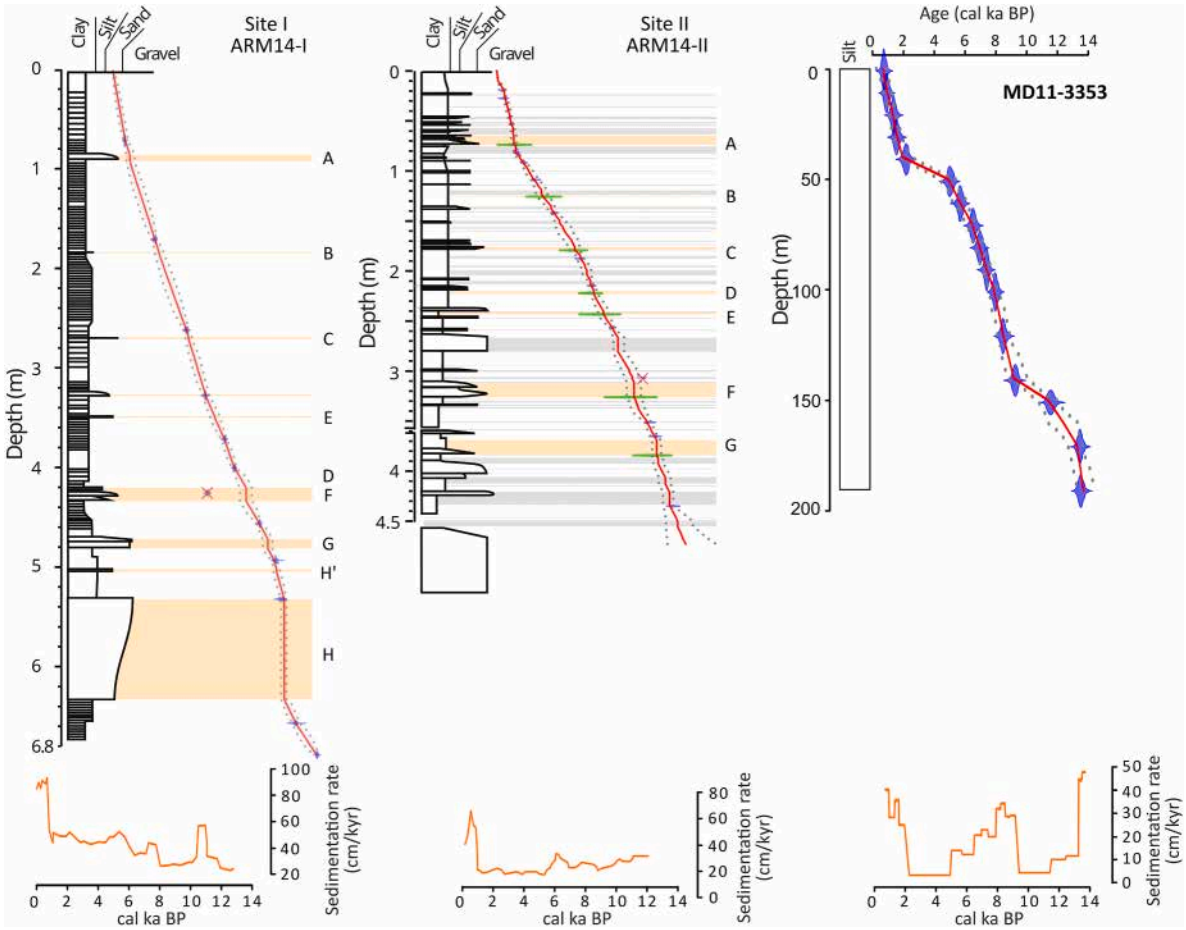

Fig. 2. Stratigraphic description and age model for the ARM14-I core (left), the one adjusted for ARM14-II core (middle) (based from Arnaud et al. (2020)) and for the MD11-3353 core (right). The blue shadings represent the calibrated ages with their distribution, the red line represents the mean age-depth relationship, and the grey dotted line represents the 95 % confidence interval. Rejected ^{14}C ages are identified by a red cross, see Table 1. Green shadings represent ages of volcanic eruptions in cal ka BP deduced by the age model of ARM14-I and taking into account in the ARM14-II age model (See Supplementary data). Capital letters identify tephra layers. Yellow stripes highlight layers interpreted as tephra deposits. Grey stripes highlight ARM14-II layers interpreted as *a posteriori* reworked volcanic material. The orange line in the lower boxes represents the sedimentation rate for each core.

2.3.3. *Extraction and analysis of biomarkers*

For biomarker analysis, 32 and 68 samples were taken from ARM14-II and ARM14-I cores, respectively. Samples were freeze-dried and homogenised, prior to lipid extraction using a Mars 6 microwave-assisted solvent extraction system (CEM Microwave Technology) with 10 mL of a mixture of dichloromethane (DCM) and methanol (MeOH), 3:1 (v/v). The extraction was repeated twice, and the total lipid extract was filtered on 20 µm Teflon filters and evaporated under a nitrogen flow. After the addition of a known amount of a synthetic C_{46} GDGT standard (Huguet et al., 2006), lipids were separated into 3 fractions by SiO_2 column chromatography. Separation was realised using 8 mL hexane (apolar fraction including *n*-alkanes), 5 mL hexane-DCM (1:1, v/v), and 10 mL DCM-MeOH (1:1, v/v) (polar fraction including GDGT).

N-alkanes from sites ARM14-I and ARM14-II were analysed at the LGL-TPE (Université Claude Bernard Lyon 1) and at EDYTEM using an HP 6890N Gas Chromatograph coupled to an Agilent HP 5975C Mass Spectrometer and a PerkinElmer Clarus 600 Gas Chromatograph coupled to a Clarus 600 T Mass Spectrometer, respectively. Both GC-MS instruments provided comparable data.

The carbon and hydrogen isotopic compositions of *n*-alkanes from site ARM14-I were measured at the LGL-TPE (Université Claude Bernard Lyon 1) using an Agilent 7890B GC coupled to an Isoprime visION Isotope Ratio Mass Spectrometer (IRMS) via an Isoprime GC-5 combustion interface (Elementar). For carbon isotope measurements, the GC-5 interface was equipped with a Quartz tube packed with CuO and operated at 850 °C. Autotuning, tests of stability and linearity of the signal were performed daily using the ionOS software. Stable carbon isotopic compositions (expressed as $\delta^{13}C$ values) were calibrated using a reference CO_2 gas reported to VPDB scale. Two mixed hydrocarbon B4 standards (A Schimmelmann, Indiana University) were measured every 4 to 5 samples and used to correct the $\delta^{13}C$ values. Samples were analysed in duplicates. For stable hydrogen isotopic compositions (expressed as δD values), the GC-5 interface was equipped with a ceramic tube operated at 1450 °C. Daily autotune, H_3^+ correction and test of stability were performed. δD values were calibrated using the reference H_2 gas reported to VSMOW. The pyrolysis furnace was regularly conditioned with hexane and the Mix hydrocarbon B4 standards were used for data correction (Schaaff et al., 2025).

Due to the low concentrations of *n*-alkanes in sediments from site ARM14-II, samples were pooled to perform δD analyses. Because of this, these pooled samples represent a greater timespan. The δD values of *n*-alkanes from site ARM14-II were measured using an online continuous flow gas chromatograph Trace-GC-Ultra coupled with an Isotopic Ratio Mass Spectrometer Delta V Plus via a pyrolysis furnace (1400 °C) and an inflow IV interface from Thermo Fischer Scientific at the ALYSES platform (IRD/SU) of the IRD Bondy. Accuracy and reproducibility of the GC-Py-IRMS measurements were assessed with an A6 standard mixture of *n*-alkanes purchased from Arndt Schimmelmann, Indiana University, of known isotopic composition. The *n*-alkane standard mixture was injected three times at the beginning of each sequence and then once

Table 2
Results of dated samples for cores ARM14-I and ARM14-II, with the radiocarbon ages and their error, the age range (minimum and maximum) calculated by the Bayesian model in rbacon (from Arnaud et al. (2020)). Samples written in italic bold are dates no used in the age models.

Core	Samples	Depth (m)	Conventional age (a BP)	Calibrated ages (cal a BP) [min-max]
ARM14I	Poz-77362	70	800 ± 40	549–903
ARM14I	SacA42461	170	2605 ± 30	2355–2858
ARM14I	SacA42462	261	4225 ± 30	4424–4961
ARM14I	Poz-77363	327	5200 ± 31	5660–6190
ARM14I	SacA42463	371	6320 ± 35	6910–7420
ARM14I	Poz-77285	400	7030 ± 40	7590–8020
ARM14I	***SacA42464***	***425***	***5335 ± 35***	***5775–6295***
ARM14I	SacA42465	456	8485 ± 45	9130–9680
ARM14I	SacA42466	493	9345 ± 45	10390–11060
ARM14I	Poz-77286	532	9580 ± 60	11250–11240
ARM14I	Poz-73369	657	10200 ± 50	11250–12460
ARM14I	SacA42467	689	11320 ± 50	12935–13450
ARM14II	SacA-122202	18	360 ± 30	−3.5-508
ARM14II	SacA-9751	26.3	425 ± 60	−5.8-652
ARM14II	Poz-69603	52	970 ± 30	679–958
ARM14II	Poz-69604	81	1297 ± 30	964–1305
ARM14II	Poz-89883	91	1775 ± 30	1429–1831
ARM14II	Poz-69605	108	2355 ± 35	2105–27018
ARM14II	Poz-69606	141	3395 ± 35	3368–3878
ARM14II	Poz-69607	187	4680 ± 40	4975–5590
ARM14II	Poz-89884	214	5340 ± 40	5760–6305
ARM14II	Poz-89885	256	6540 ± 40	7170–7580
ARM14II	***Poz-89887***	***306***	***8460 ± 50***	***9030–9655***
ARM14II	Poz-89888	351	8720 ± 50	9460–10180
ARM14II	Poz-89889	365	9090 ± 50	9765–10560
ARM14II	Poz-89891	435	9920 ± 50	10880–11760

Table 3
Equations of the different indices and transfer functions based on *br*GDGT. Roman numbers represent the relative abundance of referred *br*GDGT structures as a function of total *br*GDGT.

Index name	Equation	Reference
Isomer Ratio index	$IR_{6me} = \frac{\sum(6methyl - brGDGT)}{\sum(6methyl - brGDGT + 5methyl - brGDGT)}$	De Jonge et al. (2014a,b)
Methylation index of Branched Tetraether 5*me*	$MBT'_{5me} = \frac{I_a + I_b + I_c}{I_a + I_b + I_c + II_a + II_b + II_c + III_a}$	De Jonge et al. (2014a,b)
Cyclisation ratio of Branched Tetraethers	$CBT' = {}^{10}log\left(\frac{I_c + II'_a + II'_b + II'_c + III'_a + III'_b + III'_c}{I_a + II_a + III_a}\right)$	De Jonge et al. (2014a,b)
pH in lake	$pH = 7.15 + 1.59 \times CBT'$ $RMSE = 0.52, n = 221, R^2 = 0.85, p - value < 00001, outliers = 5$	De Jonge et al. (2014a,b)

every 3 samples. The δD is expressed in ‰ against the VSMOW. H_3^+ factor was determined daily.

For GDGT analysis, the polar lipid fraction was analysed by High Performance Liquid Chromatography coupled with an Atmospheric Pressure Chemical Ionization-Mass Spectrometer (Agilent technologies 1260 Infinity II). Chromatography separation was performed on two silica columns (BEH HILIC columns, 2.1 × 150 mm, 1.7 μM; Waters) in series (Hopmans et al., 2016). The mass/charge ratios (m/z) selected for the analysis are 744, 1303, 1300, 1298, 1296, 1294, 1992, 1050, 1048, 1046, 1036, 1034, 1022, 1020 and 1018.

2.3.4. GDGT index and temperature calibrations

Branched Glycerol Dialkyl Glycerol Tetraethers (brGDGT), produced by heterotrophic bacteria, are used for palaeothermometry, especially in lacustrine environments (Blaga et al., 2010; Castañeda and Schouten, 2011). The discovery of isomers has reduced estimation uncertainty, and the Isomer Ratio index (IR_{6me}, Table 3) quantifies their relative abundance (De Jonge et al., 2014a). The degree of methylation and the number of cycles, quantified respectively by the Methylation index of Branched Tetraether (MBT'_{5me}, Table 3) and the cyclisation ratio of branched tetraethers (CBT', Table 3), vary with temperature (Blaga et al., 2010) and pH (Raberg et al., 2021), reflecting an adaptation of cell membranes in terms of fluidity and permeability.

Previous studies have shown that seasonality, due to a drop in *br*GDGT production during winter, can bias mean annual temperature reconstructions at mid to high latitudes (Pearson et al., 2011; Shanahan et al., 2013; Q. Sun et al., 2011; X. Sun et al., 2021). New calibrations have emerged based on local rather than global datasets (Pearson et al., 2011), and/or on the mean air temperature during the Months Above Freezing (MAF) (Martínez-Sosa et al., 2021; Raberg et al., 2021; J. Zhao et al., 2022). Eventually, Zhao et al. (2023) established new transfer functions to estimate MAF for lacustrine environments, based on the global database, which we used in this study:

$$MAF = 0.19\ (\pm 0.29) + 26.49\ (\pm 0.55) \times MBT'_{5me}$$

$$RMSE = 3.13^{\circ}C, n = 552, R^2 = 0.81, p - value < 10^{-200}$$

We tested several calibrations and finally chose to present only the results computed from Zhao et al. (2023)'s equation (see Supplementary Materials, Part IV.).

2.3.5. n-alkane index

Linear normal alkanes (*n*-alkanes) with carbon chain lengths ranging from C_{27} to C_{33} are produced mainly by terrestrial higher plants (Eglinton et al., 1996; Ficken et al., 2000). In contrast, submerged aquatic plants produce *n*-alkanes ranging from C_{21} to C_{25} (Aichner et al., 2010; Liu et al., 2018; Sachse et al., 2012) whereas bacteria, algae, and fungi are characterised by even shorter chains of *n*-alkanes, $\leq C_{20}$ (Rao et al., 2009). To evaluate the relative contribution of these organisms to our *n*-alkanes record, we computed the average chain length (ACL) of *n*-alkanes ranging from C_{21} to C_{33} as follows (Poynter et Eglinton et al., 1996):

$$ACL_{21-33} = \frac{21 \times nC_{21} + 23 \times nC_{23} + 25 \times nC_{25} + 27 \times nC_{27} + 29 \times nC_{29} + 31 \times nC_{31} + 33 \times nC_{33}}{nC_{21} + nC_{23} + nC_{25} + nC_{27} + nC_{29} + nC_{31} + nC_{33}}$$

2.3.6. Interpretation of n-alkane δD values

The δD of *n*-alkanes from terrestrial plants is commonly interpreted as a proxy for temperature and/or precipitation (Jacob et al., 2007; Aichner et al., 2010; Wang et al., 2018).

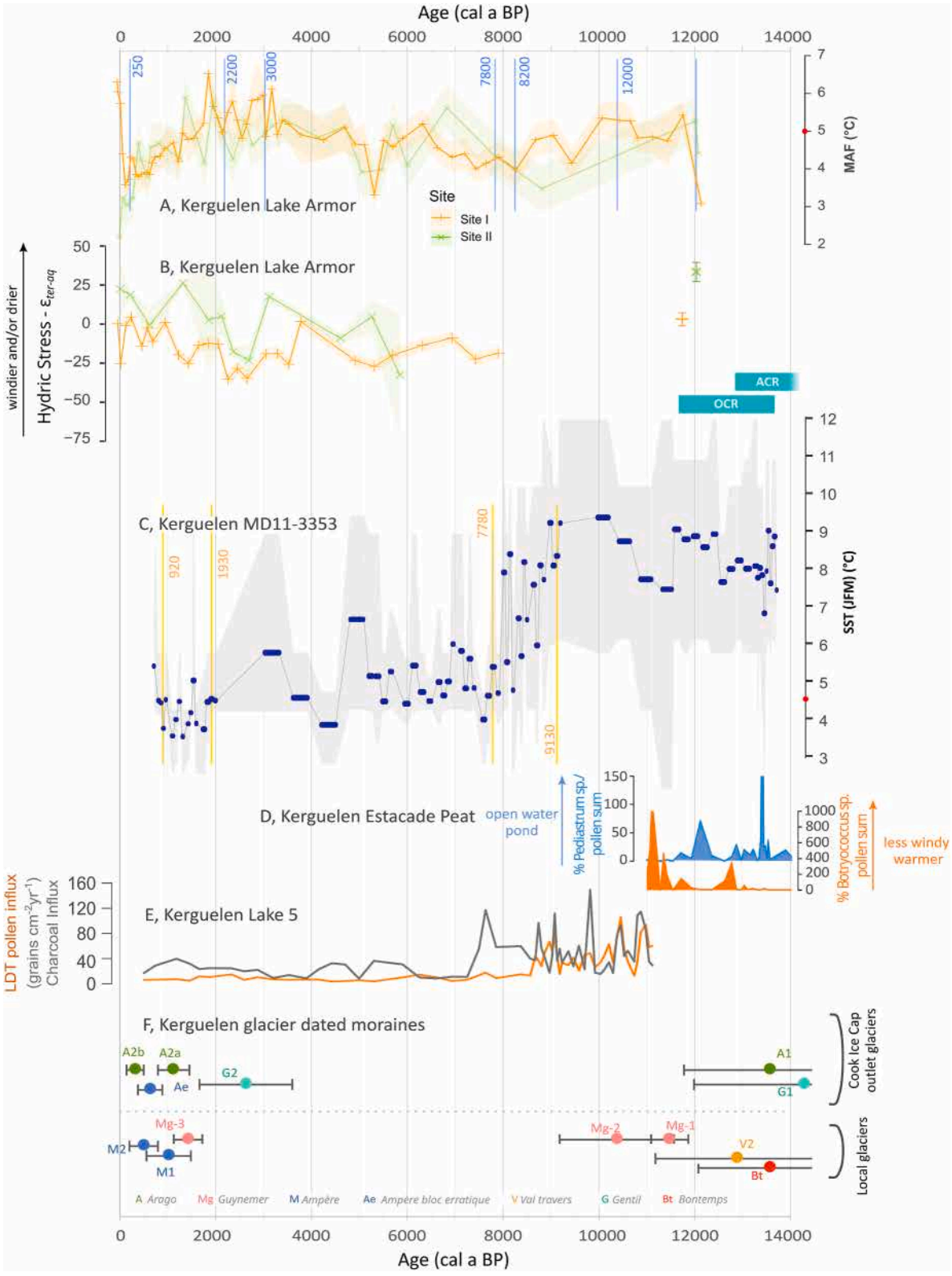

Fig. 3. Comparison of climatic variability inferred from Lake Armor with climatic regional data. A. Mean annual temperature above freezing (MAF, °C). Red point on axe represents the modern temperature. B. Hydric stress of terrestrial plants ($\varepsilon_{ter\text{-}aq}$), from Lake Armor in Kerguelen (this study). C. Summer Sea Surface Temperature (SST) from MD11-3353 (this study). The red points on the axes represent the modern ocean and air temperatures. The time span of the ACR and OCR is highlighted in blue (Stenni et al., 2001). D. Pollen abundance of *Pediastrum sp.* and *Botryococcus sp.* at Estacade peatpog (Fig. 1) used as a proxy of open water pond and, warmer and/or less windy conditions (Van der Putten et al., 2015). E. Influx of Charcoal and Long Distance Travelled pollens, from Lake 5 sediment core (Fig. 1) (Zwier et al., 2024). F. Apparent ages of moraine preserved on Kerguelen Island (Charton et al., 2022; 2022; Jomelli et al., 2017, 2018; Verfaillie et al., 2021; Tuestad et al., 2024) (Fig. 1). Vertical blue and yellow lines with the associated numbers represent ages where changes are significant according to the SiZer analysis (Chaudhuri and Marron, 1999) on MAF and SST values, respectively.

The δD values of the nC_{23} alkane mainly produced by aquatic organisms reflect those of the lake water and, consequently, of precipitation (Sachse et al., 2012), which, at high latitudes, is controlled mainly by air temperature (Huang et al., 2015). On the contrary, the *n*-alkane δD values of terrestrial plants (nC_{31}) can be affected by both temperature and evapotranspiration. The latter leads to an enrichment of the heavier isotopes in cell-water relative to the δD values of precipitation (Sachse et al., 2012). Consequently, Rach et al., and Jacob et al. (2007) used the difference between terrestrial and aquatic lipid δD values ($\varepsilon_{ter\text{-}aq}$) to correct for temperature effects and reconstruct changes in evapotranspiration, and thus in relative humidity. On Kerguelen Island, wind plays a major role as determining the environmental forcing factor. As a consequence, plant evapotranspiration processes are favoured not only by dryer conditions, but also by windier ones. Therefore, higher values $\varepsilon_{ter\text{-}aq}$, could indicate drier but also potentially, windier conditions, and *vice versa*. Note that changes in precipitation water sources do not alter this ratio.

2.4. Determination of the period for climatic palaeo-reconstruction

Palaeoclimate periods were determined using the SiZer package (Significance of Zero Crossings of the Derivative, version 0.1–8) in RStudio (Chaudhuri and Marron, 1999). SiZer was used to identify statistically significant changes in the reconstructions. By analysing the first and second derivatives, the start and end ages for each period were adjusted. This method was applied to both the MAF and SST reconstructions (for further details, refer to Supplementary Material, Part VIII).

3. Results

3.1. Marine sediment core MD11-3353

3.1.1. Age model

The core MD11-3353 age model was previously based on the comparison of the SST records and EPICA Dome C δD record (Civel-Mazens et al., 2021b; Thöle et al., 2019) with only a few tie points for the late deglaciation and Holocene periods. Based on 16 new ^{14}C ages (Table 1), we computed a new age-depth model for the uppermost 190 cm of the core, i.e., the period between 13,500 and 650 cal a BP (Fig. 2).

The linear sedimentation rate (LSR) is highly variable, ranging from ~0.004 cm/yr between 12,000 and 9000 and 5000-2000 cal a BP intervals, to ~0.5 cm/yr around 13,000 cal a BP. During the other periods of the Holocene, the LSR is around 0.02–0.04 cm/yr. As a result, the temporal resolution of the diatom counts and SST reconstruction is 500–1000 years when the LSR is lowest and ~50 years when the LSR is highest. In the other periods, the resolution is around 150 years.

3.1.2. SST reconstruction from diatoms

The reconstructed summer SSTs range between 3.5 and 9.3 °C (Fig. 3C and Fig. SM 2). With values ranging between 7 and 9 °C ocean waters around Kerguelen were much warmer between 13,600 and 9000 cal a BP than they currently are (4.5 °C). Then, they rapidly dropped to 5 °C between 9000 and 7700 cal a BP prior to experiencing a slight decreasing trend and reached ~4 °C only at 1900 cal a BP. Multicentennial variability is superimposed to those two decreasing trends. The SST difference between the two periods is significantly greater than the RMSEP of ~1.1 °C related to the calibration and the standard deviation calculated for each sample. Since 900 cal a BP, the SST have broadly increased. SiZer analysis revealed significant changes in SST at 9000, 7700, 1900, and 900 cal a BP (Fig. 3C and Supplementary Material, Part VIII).

3.2. Lake Armor sediment cores

3.2.1. Sedimentology and lithology

The two lacustrine cores present organic brownish fine mud and abundant diatom remains (Fig. 2) with interbedded mineral layers containing white volcanic pumices ranging in size from millimetre to centimetre (Arnaud et al., 2020). In ARM14-I, fibrous plant macro-remains are frequent, which is consistent with field observations of aquatic bryophytes living on the lake bottom in the perched basin, suggesting that the bottom of site I currently lies within the photic zone.

Two distinct types of interbedded mineral layers were identified (Sabatier et al., 2022): tephra deposits, which are direct atmospheric fallouts (9 layers in ARM14-I and 7 in ARM14-II), and *a posteriori* reworking of volcanic material (64 layers in ARM14-II). In ARM14-II, more interbedded layers were identified, indicating that this deep site is subject to lateral sediment inputs. We interpret them as the result of the remobilisation and redeposition of volcanic products deposited in the catchment and/or on the lake slopes surrounding site ARM14-II. The sedimentological study, combined with independent age models, allowed the correlation of the seven volcanic fallout deposits from ARM14-I with their contemporaneous deposits in ARM14-II, thus increasing the chronological match between the two sequences.

3.2.2. Age models

The ^{14}C dates of the samples are shown in Table 2 (Arnaud et al., 2020). The uppermost samples for ^{14}C dating were taken at 70 cm and 18 cm for ARM14-I and ARM14-II, respectively. The calibration curve SH-Zone 1–2 was selected (Reimer and Reimer, 2004). Two radiocarbon dates were excluded, one too old compared to the others (core ARM14-II), probably due to remobilisation and redeposition of macro-remains stored in the lake's catchment area, and the other too young in ARM14-I, possibly due to contamination during sampling (Table 2, Fig. 2).

The event layers, considered as instantaneous deposits, were removed from both sequences before age-depth modelling (Arnaud et al., 2020). The two independent age models led to the same age for direct volcanic fallout deposits within age uncertainties (2 σ) (Fig. SM 1). To assess the robustness of the age model, we carried out a cross-comparison. The ARM14-I age model was subsequently used to date all the event deposits and therefore the volcanic eruptions, due to its more homogeneous sedimentation. To adjust the ARM14-II age model, volcanic eruption ages were assigned to the corresponding tephra deposits (Fig. 2). The age gap between the age model of ARM14-II before and after adjustment ranges between −93 and 45 years, with a mean of −23 years, which is well below uncertainties.

The first 670 cm of sediment core ARM14-I and the first 450 cm of sediment core ARM14-II cover the last 13,000 and 11,500 cal a BP, respectively. For the uppermost 50 cm, the event-free sedimentation rate for ARM14-II ranges between 0.038 and 0.079 cm/yr, with a mean of 0.052 cm/yr, and for the rest of the core, it ranges between 0.015 and 0.037 cm/yr, with a mean of 0.024 cm/yr. For ARM14-I, the mean event-free sedimentation rate is 0.042 cm/yr, ranging between 0.022 and 0.062 cm/yr below 70 cm sediment depth, and increases to 0.088 cm/yr for the uppermost 70 cm, probably in relation to the higher water content of this organic-rich sediment.

3.2.3. Distribution of GDGT and inferred temperatures

Samples of Site I and Site II present a *br*GDGT distribution with a higher proportion of hexamethyl and pentamethyl compounds (50–70 % and 80–90 %, respectively) compared to tetramethyl homologues (30–50 %) (Fig. SM 5). The MBT'_{5me} index values are low and vary from 0.11 to 0.24 at Site I and from 0.08 to 0.21 at Site II (Table 3, Fig. SM 6). Using the global calibration of Zhao et al. (2023), the reconstructed temperatures range from 3.1 to 6.5 °C and from 2.2 to 5.9 °C for sites I and II, respectively (Fig. SM 6). The MAF and MBT'_{5me} reconstructions yield consistent absolute values and temporal patterns between the two

sites. The record begins with a MAF at 3 °C, prior increasing significantly to 5.5 °C until 10,600 cal a BP and decreases slightly to 10,300 cal a BP (Fig. 3A). To discuss the significant changes in the index and MAF variation, the SiZer package has been used. According to SiZer, in the long term, the cooling started at approximately 9900 cal a BP and ended at 8250 cal a BP, when MAF reached 4 °C (Fig. 3A). Then, MAF increased again to reach its maximum value of around 6.5 °C at 1900 cal a BP (Fig. 3A). Regarding mid- and short-term trends, the warming began significantly at 7700 cal a BPcal a BP and at 8000 cal a BP, respectively, and stopped at 3000 cal a BP (Fig. SM 13). Between 3000 and 2000 cal a BP, the MAF remained high, around 5 °C, but with important variations (Fig. 3A). Afterwards, cooling started significantly at 2600 cal a BP, with a moderate-term age trend (Fig. SM 13), to reach 3 °C. However, this cooling became more pronounced at 2200 cal a BP, according to the analysis of the second derivative with SiZer (Fig. SM 13). Finally, the increase in MAF at the end of the record is significant in the short term.

At sites I and II, IR_{6me} ranges from 0.15 to 0.42 and from 0.19 to 0.31, respectively; the CBT' values range from −0.73 to −0.15 and from −0.64 to −0.32, respectively (Table 3, Fig. SM 6), which are translated into pH values varying from 6.0 to 6.9 and from 6.1 to 6.6, respectively (Table 3, Fig. SM 6) (De Jonge et al., 2014a).

In contrast to MAF values, pH variations are different at the two sites between 1000 and 4000 cal a BP (6.6 for Site I and 6.4 for Site II) (Fig. SM 6). The correlation between MBT'$_{5me}$ and MAF is influenced by the pH (De Jonge et al., 2014b; Raberg et al., 2021) when the IR_{6me} is higher than 0.5 (Bauersachs et al., 2024), which is not the case in the Armor records (See Supplementary Material, Part V, for more details).

3.2.4. *n*-Alkane distributions, concentration and stable hydrogen isotopic composition

The total *n*-alkane concentrations range from 2.81 to 79.66 μg/g and 1.92–25.26 μg/g of dry sediment at sites I and II, respectively. In both cores, the most abundant *n*-alkanes are the nC_{25} and nC_{27} (Fig. SM 11). The $ACL_{21\text{-}33}$ values vary between 23.9 and 28.1, and between 25.8 and 28.8, for sites I and II respectively (Fig. SM 8). The values on Site I are lowest at the beginning of the sequence, around 11,000 cal a BP, and increased to around 26.7 between 10,000 and 1000 cal a BP, except between 8200 and 7000 cal a BP when they decrease to *ca*. 26.0 (Fig. SM 8). The values then rose again until 6000 cal a BP, reaching 28.1, at the most recent part of the record, potentially indicating an increasing influence on terrestrial sources (Poynter and Eglinton, 1990). The *n*-alkane sediment core composition is produced by two main groups. The first one is aquatic, composed of micro-organisms and submerged plants, which produce mid-length chains of *n*-alkanes (nC_{21} and nC_{23}). The second are the terrestrial higher plants, which produced long-length chains *n*-alkanes (nC_{31} and nC_{33}, including nC_{29} for Site II) (See Supplementary Material, Part V, for more details on *n*-alkane sources).

The hydrogen isotope values, δD, of nC_{23} ranged from −184 to −137 ‰, and from −183 to −118 ‰ for sites I and II, respectively. δD nC_{31} values range between −177 and −150 ‰; and −166 and −141 ‰, for sites I and II, respectively (Fig. SM 8).

For Site II, the $\varepsilon_{ter\text{-}aq}$ values are higher than those for Site I, ranging from −32.6 ‰ to 26.3 ‰, and from −35.5 ‰ to 4.5 ‰, respectively (Fig. 3B). Owing to the low resolution of the isotopic data for Site II, it is difficult to assess the similarity between the two trends, although a degree of similarity can be observed in the variations in $\varepsilon_{ter\text{-}aq}$.

3.2.5. Consistency between the two lacustrine cores

The difference between the two age models of ARM14-II is smaller than the associated age uncertainty. Therefore, the two cores could be considered dated independently. Moreover, the two sediment cores were sampled in two different sedimentary environments. This specific methodology allowed us to question and confirm the reproducibility of reconstructed parameters across two independent sequences. We are therefore highly confident in the climatic interpretations of the proxy records.

Similar trends and ranges are observed in the GDGT-derived temperatures and δD values of *n*-alkanes for cores ARM14-I and ARM14-II (Figs. SM 6, 8). The lower concentrations in *n*-alkanes at Site II, due to its location below the photic zone, generate low resolution and large uncertainties in δD measurements, and therefore more discrepancies between the two sites for this particular proxy.

4. Discussion

4.1. Integration of Lake Armor data into Kerguelen climate reconstructions

In the absence of air temperature reconstructions, previous studies of Kerguelen glacier fluctuations have relied on the assumption that these variations reflect changes in SST (Charton et al., 2022). Our results led us to reconsider this assumption thanks to quantitative air temperature as well relative precipitation and/or wind regime reconstructions. We also based our interpretation on the framework of palaeovegetation records, which provide additional information on qualitative air temperature, moisture conditions and the latitudinal position of SHW (Van der Putten et al., 2015; Zwier et al., 2024).

4.1.1. The end of the late glacial period (16,000 to 11,500 cal a BP)

Quantitative sea water (SST) and air temperatures (MAF) can only be directly compared over the last 12200 years, i.e. the oldest information we have from Lake Armor. We hence used qualitative air temperature information from the Estacade peat bog record (Van der Putten et al., 2015), located in the northeastern part of Kerguelen (Fig. 1), for periods before 12,200 cal a BP.

At 16,000 cal a BP, warm SST values were prevailing (approximately 6.5°C, Civel-Mazens et al., 2021b), which is consistent with the relatively warm and wet conditions deduced from the Estacade record (Van der Putten et al., 2015).

During the late glacial periods, our records appear to catch two cold events which were observed in the ice cores of Dome C: the Oceanic Cold Reversal between 13,600 and 11,650 cal a BP (OCR, in the precipitation moisture source, *i.e.* South of the Indian Ocean) and the Antarctic Cold Reversal between 14,550 and 12,800 cal a BP (ACR, in Antarctica) (Stenni et al., 2001; Van der Putten et al., 2015). Indeed, toward the end of the ACR period and the beginning of the OCR, colder SST appeared to prevail near the Kerguelen Islands (8 °C between 13,400 and 12,500 cal a BP, *i.e.* 1° less than that in the following periods) (Fig. 3C). By this time, wetter conditions were recorded at Estacade, inducing an increase in open water pond size (Van der Putten et al., 2015, Fig. 3D), and evidence of multiple glacier advances were reported (Charton et al., 2022, Fig. 3F). However, the major cold and wet event occurred between 13,600 and 12,900 cal a BP, congruent with the OCR (Fig. 3C). Thereafter, SSTs from MD11-3353 reached a maximum of 9 °C at 10,000 cal a BP (Fig. 3C).

In contrast, Lake Armor MAF had the lowest air temperatures on record, e. g, ~3 °C at 12,200 cal a BP (Fig. 3A), however, more data is needed. Then MAF rose to 5 °C by 11,600 cal a BP, in accordance with the slight warming recorded at Estacade at 11,600 cal a BP (Van der Putten et al., 2015).

The $\varepsilon_{ter\text{-}aq}$ values were high at 11,700 cal a BP, suggesting an important hydric stress for terrestrial plants due to dry conditions and/or strong winds (Fig. 3B). As Van der Putten et al. (2015) suggested less windy and drier conditions (Fig. 3D), our δD record could hence reflect dry conditions. However, this observation at Armor must be taken with caution, as it is based on two samples only, from two different cores (Site I and Site II).

4.1.2. Early Holocene (11,500–9000 cal a BP)

A warm period occurred between 11,500 and 10,000 cal a BP. Both SST and MAFs reach an Early Holocene maximum of 9.2 °C and 5.2 °C, respectively (Fig. 3A–C). This is consistent with multiple evidence of

glacial retreats: a peat bog deposit dated to 10,220 ± 90 a BP (*i.e.* 11,840 ± 560 cal a BP using the Southern Hemisphere SHCal20 radiocarbon calibration curve (Hogg et al., 2020)), and several boulders whose exposure ages were dated with ^{36}Cl between 11,100 ± 300 a BP and 10,400 ± 400 a BP at Col Louise (Tuestad et al., 2024). At Kerguelen, this period is currently defined as a climatic optimum (Civel-Mazens et al., 2021a; Frenot et al., 1997 ; Labracherie et al., 1989; Young and Schofield, 1973; Zwier et al., 2024).

During this period, both the air and sea surface temperatures slightly decreased between 11,600 and 10,500 cal a BP (Fig. 7A–C). This coincides with the advance of a local glacier located north of the island (Glacier Guynemer; Tuestad et al., 2024), whereas there is no evidence of a contemporary advance of any of the Cook ice-cap tongues (Fig. 3F). This local glacier advance, during a period of relatively high temperature (MAF = 5.2 °C, compared with 6 °C at the current time), suggests a control by precipitation. Unfortunately, we were not able to get δD data for this period to corroborate this hypothesis (Fig. 3B).

4.1.3. 9000 cal a BP: an important cooling event

Around 9000 cal a BP, the transition between the Early Holocene temperature optimum and the Mid-Holocene period was marked by a drastic drop in both sea water (from 9 °C to 4.5 °C) and air (from 5 °C to 6 °C) temperatures (Fig. 3A–C). At that time, the SAF and APF migrated northwards (Civel-Mazens et al., 2021b). Zwier et al. (2024) described an abrupt coeval decrease in a long-distance pollen influx, which they attributed to an African source (Fig. 3E). Whereas the drop in air temperature is less marked than the one in SST (Fig. 3A–C), our findings point to a concomitant shift in air-mass trajectories (Fig. 3E) and an oceanic water-mass organisation. A continuous rise in air temperature from 8000–3000 cal a BP.

At 8000 cal a BP, the MAF temperature shows a progressive warming trend from 4 to ~6 °C (Fig. 3A). Zwier et al. (2024) inferred a stable and relatively cold Mid-to Late Holocene climate, based on the absence of changes in local plant taxa. Moreover, although the retreat of the Ampère Glacier at 5140 ± 340 cal a BP (recalibrated with SHCal20) has been reported (Frenot et al., 1997), most studies reported no clear evidence of glacier advance during the Mid-Holocene (Charton et al., 2021, 2022; Jomelli et al., 2017) (Fig. 3F). Our data hence confirm the idea of a relatively cold Mid-Holocene, but not sufficiently cold and/or humid enough to drive a detectable extension of the Cook ice-cap (Charton et al., 2021, 2022; Frenot et al., 1997; Jomelli et al., 2017).

During the Mid-Holocene, an abrupt 1 °C cooling in air temperature occurred at 5200 cal a BP (Fig. 3A). This cooling is concomitant the interpretation derived from a pollen record (Young and Schofield, 1973) and various moraine boulders, which were, however, considered as outliers because their ages were inconsistent with the rest of the moraine records (Tuestad et al., 2024). Despite the agreement among several proxies and records, further investigation remains necessary to confirm the reality of this cold period, as we observed it in Lake Armor for only three data points.

Overall, our data provide the first evidence of a progressive warming of 1 °C within 6000 years, culminating around 3000 cal a BP. Interestingly, this trend accompanies an opposite one in SST, which dropped by 1 °C over the same period.

4.1.4. The Late Holocene regional Hypsithermal (3000–2000 cal a BP)

The Lake Armor record provides novel evidence in favour of a temperature maximum, which occurred between 3000 and 2000 cal a BP. MAF values then stabilised at approximately 5.5 °C, i.e. 0.5 °C above the currently observed data and 0.5 °C below the highest values of our reconstruction, with variations of less than 1 °C in amplitude (Fig. 3A). This interval represents the warmest period of the entire Holocene, except modern values, in agreement with the definition of regional Hypsithermal (De Deckker, 2022). Conversely, the SST remained relatively cold (~5 °C) during this period with some variability (Fig. 3C). Our results are in agreement with the continuous reconstruction of

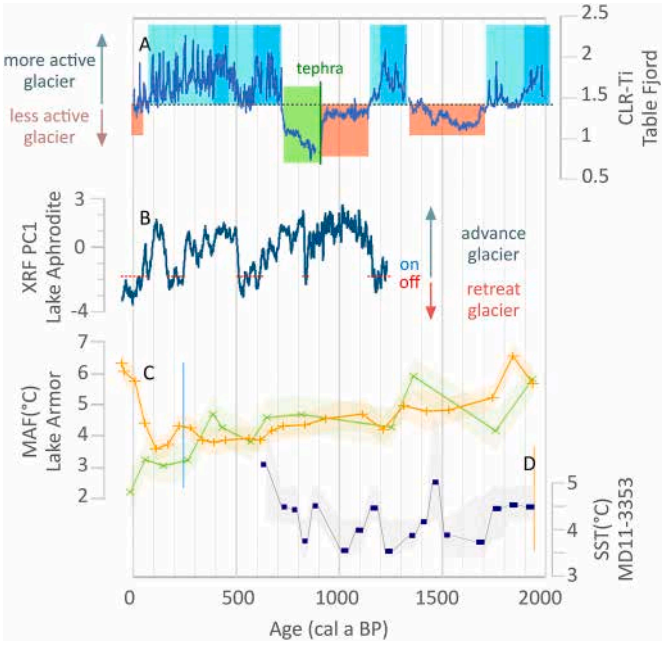

Fig. 4. Comparison of climatic variability inferred from Lake Armor with climatic regional data over the past 2000 years. A. Centred log-ratio of Ti content (CLR-Ti) in the sediment record from Table Fjord inferred as Ampere Glacier advance/retreat (Fig. 1A–Chassiot et al., 2024). Blue/Red areas indicate periods when Ampere Glacier's size increased/decreased. Green stick and area represent the position of the tephra layer when data is unusable. B. Reconstruction of Chamonix Glacier advances based on the X-ray fluorescence Principal Component 1 (XRF-PC1) in the record from Lake Aphrodite (Sleire et al., 2025). The red dashed lines represent the threshold above which the Chamonix Glacier advanced. C. Mean annual temperature above freezing (MAF, °C) D. Hydric stress of terrestrial plants ($\varepsilon_{ter\text{-}aq}$), from Lake Armor in Kerguelen (this study). Vertical blue and yellow lines represent ages where changes are significant according to the SiZer analysis (Chaudhuri and Marron, 1999) on MAF and SST values, respectively.

Ampère Glacier dynamics, derived from terrigenous inputs into Baie de la Table, which suggests a glacier retreat between 2800 and 2300 cal a BP (Chassiot et al., 2024). In addition, from 3500 to 1500 cal a BP, $\varepsilon_{ter\text{-}aq}$ reached its lowest value (−35 ‰), potentially indicating lower hydric stress, meaning drier or windier conditions (Fig. 3B). Those warm, but wet, conditions could explain a glacial advance of the Gentil Glacier, dated 2620 ± 970 cal a BP (Fig. 3F) (Charton et al., 2021). Indeed, Charton et al. (2021) suggested that this advance was made possible by i) its rocky debris cover, which insulates the ice and protects it from melting, and ii) an increase in precipitation that sustains the glacier, allowing it to advance despite a potentially warm period.

4.1.5. Cold period and regional Little Ice Age (2000–250 cal a BP)

Between 2000 and 250 cal a BP, the MAF cooled by 2 °C, whereas the SST varied around 4 °C (Fig. 3A and B). At Kerguelen, several lines of evidence for glacier advances and colder conditions have been inferred (Fig. 3F) (Charton et al., 2021, 2022; Chassiot et al., 2024; Frenot et al., 1997; Jomelli et al., 2017, 2018; Sleire et al., 2025; Tuestad et al., 2024; Young and Schofield, 1973). This is also consistent with the advances of the Chamonix Glacier (1150–250 cal a BP, Sleire et al., 2025) and the Ampère Glacier (from 2300 cal a BP; moraines dated to 800 ± 260 a BP and 580 ± 310 a BP; Chassiot et al. (2024); Verfaillie et al. (2021)). However, these advances were interrupted during two distinct periods: 850–820 cal a BP and 620–500 cal a BP for the Chamonix Glacier, and 1700–1300 cal a BP and 1150–1000 cal a BP for the Ampère Glacier (Chassiot et al., 2024; Sleire et al., 2025). The causes of these retreat phases remain unexplained.

The rise in $\varepsilon_{ter\text{-}aq}$ values (from −25 to 5 ‰ from 1600 to 100 cal a BP)

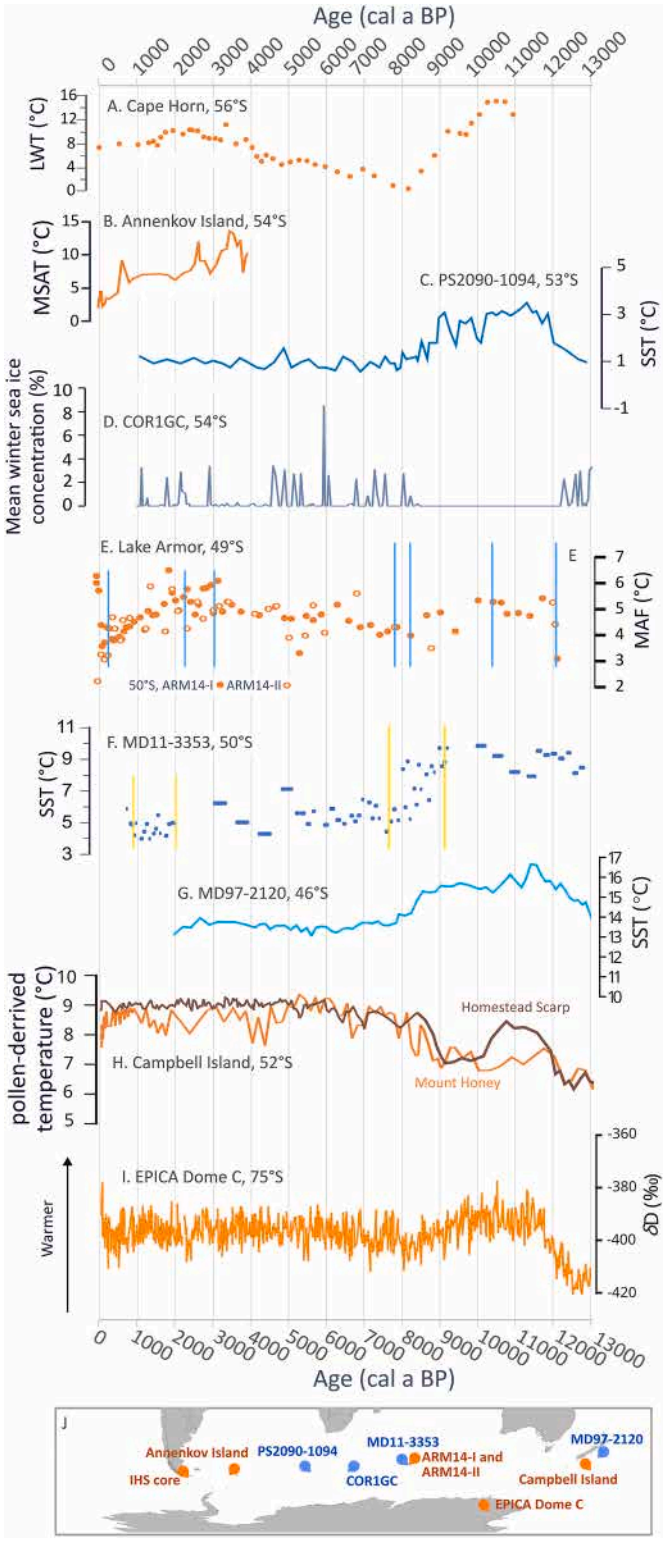

Fig. 5. Comparison of temperature variability over the Southern Hemisphere. In orange/brown continental records. In blue oceanic records. A. Lake Water Temperature (LWT,°C) at Hornos Island in Cape Horn (Perren et al., 2025). B. GDGT-derived temperature Mean Summer Air Temperature (MSAT) from a sediment core of the Fan Lake (FL), Annenkov Island (near South Georgia) (Foster et al., 2016). C. Diatom-based Sea Surface Temperature (SST)-record in sediment core PS2090-1094 from the South Atlantic (Bianchi and Gersonde, 2004). D. winter mean sea-ice concentration record based on diatom assemblages from COR1GC in the Indian Ocean (Orme et al., 2020). E. Mean annual temperature above freezing (MAF, °C) from Lake Armor (Kerguelen, this study). F. Diatom-based Sea Surface Temperature (SST)-record in sediment core MD11-3353 off the coast of Kerguelen (this study). Vertical blue and yellow lines represent ages where changes are significant according to the SiZer analysis (Chaudhuri and Marron, 1999) on MAF and SST values, respectively. G. Alkenone-based SST record in sediment core MD97-2120 at east of New-Zealand (Pahnke and Sachs, 2006). H. Pollen-based temperature derived at Mount Honey and Homestead Scarp, Campbell Island McGlone et al., 2010. I. δD (‰SMOW) record from EPICA Dome C (Stenni et al., 2010). J. Map of the Southern Hemisphere showing the locations of the different records discussed in this study.

Table 4
Time span of bins used in function of the period considered.

Period (cal a BP)	Bin time span (yr)
Present – 1650	300
1650–9950	450
9950–11,200	650
11,200–13,000	850

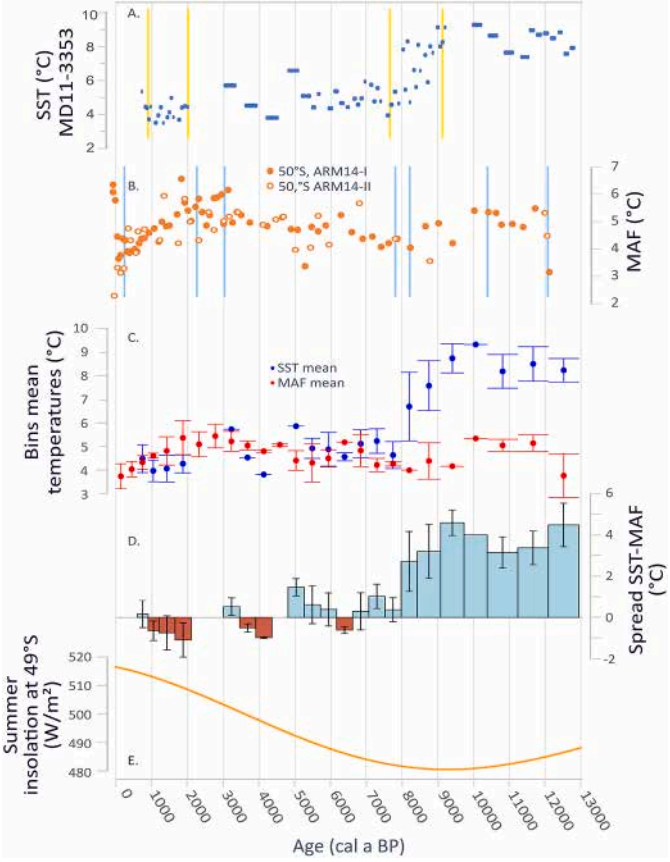

Fig. 6. Comparison of atmospheric and sea surface temperature at Kerguelen. A. Diatom-inferred summer sea surface temperature (SST) from MD11-3353 (this study). B. Mean annual temperature above freezing (MAF) from Lake Armor in Kerguelen (this study). C. Mean MAF and mean SST with their standard deviation calculated for each bin. D. Spread between oceanic and atmospheric mean temperatures over time for the Kerguelen area. E. Summer insolation (W/m^2) at 49°S computed thanks to the package *palinsol* (version 1.0) with Rstudio software (Berger, 1978). Vertical blue and yellow lines represent ages where changes are significant according to the SiZer analysis (Chaudhuri and Marron, 1999) on MAF and SST values, respectively.

shows no evidence of a decrease in hydric stress (Fig. 3B). An increase in precipitation is needed for important glacier advances (Charton et al., 2022). Therefore, these findings may indicate that windier conditions compensated for the increase in humidity maintaining continental plants under hydric stress.

4.1.6. Current warming

From 250 cal a BP to the present day, our data clearly show warming, with air temperatures increasing from around 3.5 to 6 °C (Figs. 3A and 4C, Fig. SM 17). During the instrumental period, *i.e.* since 1950 CE, we computed the MAF from Port-aux-Français weather station data. Despite the lack of resolution of our reconstructed temperatures, both series (instrumental measurements and reconstituted temperatures at Site I) show similar trends, with an offset of *ca.* 1 °C (Fig. SM 17). Despite a reported short-term advance of the Chamonix Glacier between 160 and 190 cal a BP (Chassiot et al., 2024), the last 300 years were marked by a net retreat of glaciers both in Kerguelen and throughout the whole Southern Hemisphere (Charton et al., 2021, 2022; Favier et al., 2016b; Jomelli et al., 2021; Verfaillie et al., 2015, 2021) (Figs. 3F and 4).

Since 250 cal a BP, $\varepsilon_{ter\text{-}aq}$ data indicate windier and/or drier conditions, which is in agreement with the drying trend observed at the Port-aux-Français weather station, and with Favier et al.'s (2016a,b) conclusions based on glacier modelling. However, potential micro-organism community changes (see Section 4.2.2.) warrant caution with the interpretation of $\varepsilon_{ter\text{-}aq}$, without other independent data.

4.2. Comparison over the Southern Hemisphere

At Cape Horn (55.97°S), Perren et al. (2025) reconstructed the Holocene lake water temperature (LWT), using isoprenoid GDGT (Fig. 5A). Comparable temperature variations are observed in the Cape Horn and Lake Armor records; however, the amplitude of these variations is smaller in the Lake Armor record. This remarkable consistency suggests that the biomarkers reflect robustly large-scale changes, rather than local variability.

Early Holocene warm conditions were reported across the entire Southern Hemisphere. Around subantarctic islands Crozet and Heard, the SST values were high between 11,000 and 10,000 cal a BP (MD73-025, MD84-527, Labracherie et al. (1989)). South of the Conrad Rise (54.26°S, 39.76°E), the absence of winter sea ice and particularly warm diatom-derived SSTs are documented between 8600 and 11,600 cal a BP (Orme et al., 2020) (Fig. 5D). During the Early Holocene, a climatic optimum has been documented in the Indian basin (Civel-Mazens et al., 2021a; Frenot et al., 1997; Labracherie et al., 1989; Young and Schofield, 1973; Zwier et al., 2024), South America (Perren et al., 2025; Saunders et al., 2018; Zwier et al., 2022), and Antarctic ice cores from Vostok, EPICA Dome C (EDC), and Maud Land (EDML) (Ciais et al., 1994; Stenni et al., 2010) (Fig. 5). By contrast, Campbell Island did not record maximum pollen-derived temperatures during the Early Holocene, instead showing a marked cooling between 11,000 and 9200 cal a BP (McGlone et al., 2010, 2019) (Fig. 5H).

An abrupt cooling event (9000-8000 cal a BP) is recorded across multiple sectors. It began nearly simultaneously at ~9200 cal a BP in the Indian sector of the Southern Ocean (Labracherie et al., 1989) and ~9000 cal a BP in the Atlantic (Bianchi and Gersonde, 2004; Nielsen et al., 2004) (Fig. 5C) and in the western Pacific (Pahnke and Sachs, 2006) sectors (Fig. 5G).

For the Mid- and Late Holocene, more discrepancies are observed. Like in Lake Armor records, a climate optimum was documented in the Antarctic Peninsula between 4500 and 3000 cal a BP (Ingolfsson et al., 2003). In contrast to Armor records, Ooms et al. (2011) and Van der Putten et al. (2008) inferred persistent cooling, in the Indian Ocean, from 6000 to 3000 cal a BP and from 5500 to 4600 cal a BP, respectively. As in Armor, at Cape Horn and Annenkov Island (GDGT-derived temperature in a peat core, near South Georgia, 54°S), Perren et al. (2025) and Foster et al. (2016) reported warm conditions until ~2500 cal a BP, followed by gradual cooling (Fig. 5A and B). However, unlike Perren et al. (2025) and the Armor record, Foster et al. (2016) identified a 1200–600 cal a BP warm peak, interpreted as a regional expression of the Medieval Climatic Anomaly (Fig. 5B). Nevertheless, the Late Holocene cold period (2000-250 cal a BP) was characterised by a major, widespread period of glacier advance (Charton et al., 2021, 2022; van der Bilt et al., 2017; Xia et al., 2020) (Figs. 3F and 4). These periods encompass the regional Little Ice Age (regional LIA, 380-220 cal a BP) previously observed in South Georgia (54 °S) (van der Bilt et al., 2017). However, in Antarctica, the occurrence and timing of a LIA are still debated (Simms et al., 2012). Moreover, the Late Holocene cold period corresponds to a decrease in Antarctic atmospheric temperature of around 2500 cal a BP (Mulvaney et al., 2012; Sterken et al., 2012; Totten et al., 2015) and to the onset of the most recent Neoglacial period, which

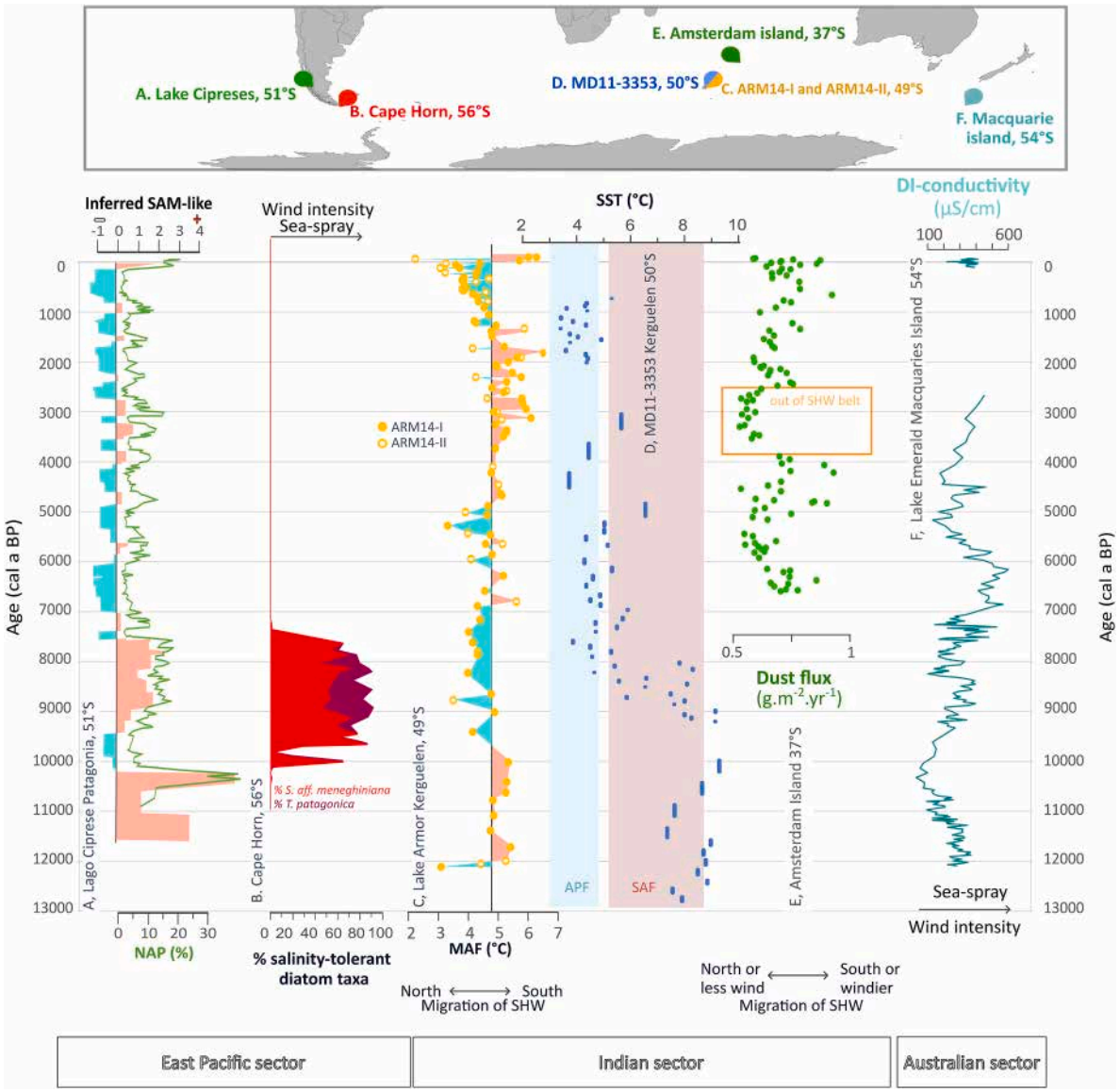

Fig. 7. Comparison of SHW variability on strength and/or latitudinal migration over the Southern Hemisphere during the Holocene. **A.** Abundance of Non-Arboreal Pollen (NAP) inferred in SAM-*like* indice in Lago Cipreses in Patagonia (Moreno et al., 2014). **B.** Percentage of salinity-tolerant planktonic diatom species (*Stephanocyclus aff. meneghiniana* and *Thalassiosira patagonica*), indicating increased wind strength at Hornos Island, Cape Horn (Perren et al., 2025). **C.** Mean annual temperature above freezing (MAF) from Lake Armor in Kerguelen (this study). Red/blue areas indicate periods of positive/negative SAM-*like* periods determined by whether the values are above/below the Holocene mean MAF. **D.** Diatom-inferred summer sea surface temperature (SST) from MD11-3353 (this study). Vertical bands cover the surface temperature observed for the oceanic fronts. SAF: Sub-Antarctic Front. APF: Antarctic Polar Front. **E.** Dust flux in peat core of Amsterdam Island (Li et al., 2020). The orange box indicates a period during which we hypothesise that the study area was not subject to the influence of SHW. The double-arrow represents the SHW latitudinal migration inferred from C and E. **F.** Diatom-inferred (DI) conductivity in the Lake Emerald on Macquarie Island (Saunders et al., 2018).

began at around 2500 cal a BP (Totten et al., 2015), although its timing remains debated (Simms et al., 2012).

4.3. Air vs. oceanic temperatures

Based on the observed correlation between air and sea surface temperatures over recent decades (Favier et al., 2016b), Charton et al. (2022) inferred that palaeo-SST are a reliable proxy for past air temperatures. Moreover, Xia et al. (2020) interpreted a shift in air temperature from Foster et al. (2016) as the result of a Antarctic Polar Front (APF) migration near the island, implicitly suggesting that SST and air temperature were correlated. In line with this reasoning, Perren et al. (2025) hypothesised that air temperature variations during the Mid- and Late Holocene at Cape Horn Island reflect the surrounding SST variations.

The lack of local air temperature records led several authors to compare their findings with remote records, such as those from West Antarctica (Charton et al., 2021; Jomelli et al., 2017) or Patagonia. However, because there is no evidence that temperature patterns around the Southern Hemisphere are uniform (Charton et al., 2021, 2022), closest SST records are often considered as reliable indicators of local air temperature, and *vice versa*. Our dataset provides a unique opportunity to compare independent air and sea surface temperature records in a restricted area where similar climatic and oceanographic conditions prevail. To this end, we computed the spread between two variables: diatom-derived SSTs and GDGT-derived MAFs. To account for the different sampling steps of our records and make our SST-MAF spread signal more robust, we defined different time bins. The timespan of

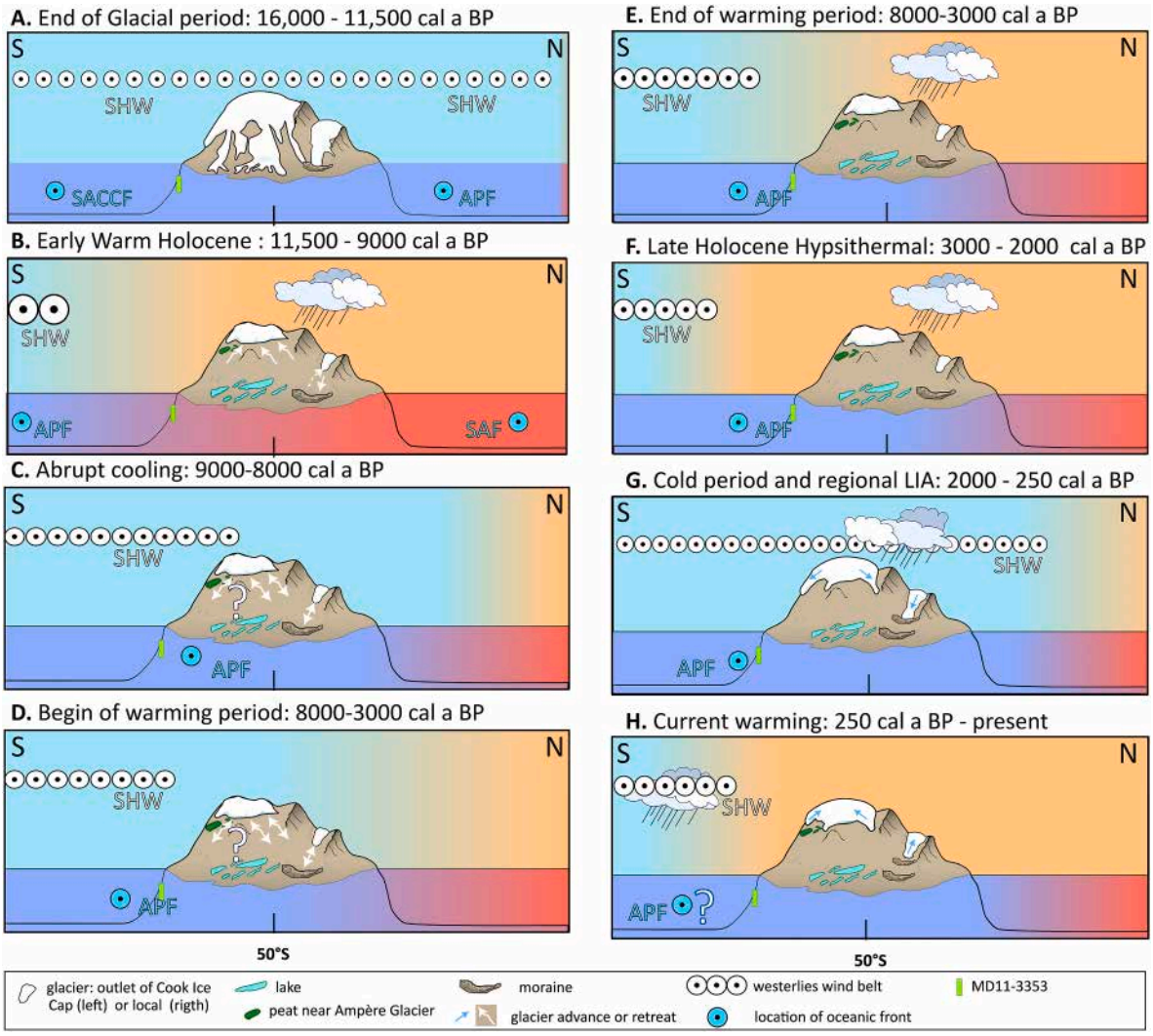

Fig. 8. Schematic representation of latitudinal migration of oceanic and atmospheric fronts during different key periods and their implication on Kerguelen glacier fluctuation and the formation of the lake. Note the size of frontal arrows for SHW indicates the intensity of the wind and only surface water are discussed. The represented peat corresponds to the one found near the Ampère Glacier (Frenot et al. 1997). Red/orange colors indicated warm sea surface/air temperatures Blue colors indicate colder temperatures. Question marks indicate when we do not know the location of the front oceanic or the movement of glacier. SHW: Southern Hemisphere Westerlies. SACCF: Southern ACC Front. APF: Antarctic Polar Front. SAF: Sub-Antarctic Front. LIA: Little Ice Age.

selected bins is larger than the mean age uncertainty of the samples that compose it. Accordingly, it is greater for the Early than the Mid-Holocene (Table 4). They have been adjusted to be sufficiently long to allow meaningful analysis without overinterpreting the data, yet short enough to preserve good temporal resolution over the past 12,000 years. In each bin, the averages of MAF and SST were calculated and the difference between them was computed (Fig. 6C). For bins whereas one of the temperature means was missing, no SST-MAF spread data were calculated (Fig. 6D).

Although the land and marine temperatures at Kerguelen displayed broadly similar trends, their relationships varied significantly throughout the Holocene (Fig. 6A and B). The SST-MAF spread was the highest during the Late Glacial-Early Holocene period (4 °C, Fig. 6D), when insolation at 50°S presented a minimum (Fig. 6E). Therefore, we infer that low insolation counterbalanced high surrounding sea temperature to keep air temperature within the range that is currently observed, whereas SST were 5 °C above their current values. During the 9000 cal a BP cooling, the spread values remained large from 9500 to 7950 cal a BP due to large variations in SST, before reaching a minimum between 6150 and 6600 cal a BP (Fig. 6D). Over the last 8000 years, the SST-MAF spread has varied between −1 and +1 °C, suggesting a stronger relationship between marine and air temperatures than during the Early Holocene (Fig. 6D). A trend toward more frequent negative spreads (*i.e.* air temperature > SST) has also been observed since 6300 cal a BP (Fig. 6D). However, the variations in the MAF we identified are not clearly mirrored in the SSTs over the last 8000 years (Fig. 6A and B). Consequently, it appears that SSTs are not a good predictor of air temperatures on the Kerguelen Islands over the whole Holocene, in contrast to the Cape Horn region (Perren et al., 2025). On the basis of 50 years of historical and modern measurements at Port-aux-Français and over Kerguelen, respectively, Pohl et al. (2021) consistently concluded that current terrestrial climates are largely shaped by atmospheric systems, such as the Southern Annular Mode (SAM), rather than oceanic or coupled climate modes. Therefore, the strong correlation observed at Port-aux-Français between SST and MAF values (Favier et al., 2016a; Pohl et al., 2021) is not representative of the entire island (Pohl et al., 2021).

4.4. Southern Annular Mode patterns in the Indian ocean during the Holocene

The SHW belt separates two atmospheric masses: a warmer air mass

to the north from a colder one to the south. At Kerguelen, this boundary is sharply delineated (Pohl et al., 2021), so any latitudinal shift in the SHW belt directly affects local air temperature. A southward shift warms the atmosphere, while a northward shift cools it, as shown by historical data (Gillett et al., 2006), reanalyses (Fogt and Marshall, 2020b; Hersbach et al., 2019) and models (Sijp and England, 2008). The SAM index, calculated as the anomaly in the atmospheric pressure difference between 40 and 65°S (Thompson and Wallace, 2000) reflects those latitudinal migrations. A positive (negative) SAM index reflects a poleward (equatorward) shift in the SHW belt, accompanied by stronger (weaker) wind (Marshall, 2003; Gillett et al., 2006; Jones et al., 2009).

Palaeoclimate studies have proposed SAM reconstructions on multidecadal to multicentenial scales (Fletcher and Moreno, 2012; Lamy et al., 2010; Li et al., 2020; Moreno et al., 2010, 2014, 2018, 2021; Saunders et al., 2018; Spoth et al., 2023; Villa-Martínez and Moreno, 2007; Zwier et al., 2024). However, as the pressure gradient cannot be reconstructed directly, Moreno et al. (2018) suggested referring to a 'SAM-like' processes.

Here, we assume that positive air temperature anomalies at Kerguelen reflect predominantly positive SAM-like conditions, *and vice versa* (Fig. 7). Fig. 8 summarises Kerguelen palaeoclimate observations and their implications for atmospheric and oceanic dynamics in the Mid- to High-latitude Southern Indian Ocean.

4.4.1. *Positive SAM-like periods*

In the Lateglacial/Early Holocene (12,200 to 10,000 cal a BP), we infer a major positive SAM-*like* period (Figs. 7C and 8B), as both the wind belt and the Antarctic Circumpolar Current (ACC) fronts migrated southwards. High SST suggest that even the Subantarctic Front (SAF) could have shifted south of Kerguelen (Ai et al., 2024) (Fig. 7D); despite contradictory information derived from radiolarian assemblages (Civel-Mazens et al., 2021a). The Agulhas Return Current also shifted southward despite a weaker flow (Civel-Mazens et al., 2021a). African pollen presence in Lake 5 record (northern Kerguelen, Fig. 1A), was interpreted as a sustained positive SAM-like phase during the Early Holocene (Fig. 3E) (Zwier et al., 2024). It was also documented in southern Patagonia (McCulloch et al., 2023; Moreno et al., 2014, 2018, 2021; Villa-Martínez and Moreno, 2007), Cape Horn (Perren et al., 2025), Falkland Islands (Spoth et al., 2023), the Atlantic sector of the Southern Ocean (Bianchi and Gersonde, 2004), the Australian region (McGlone et al., 2019; Moreno et al., 2018, 2021; Perren et al., 2025; Saunders et al., 2018), and the African sector (reviewed in Fletcher and Moreno, 2012) (Fig. 7A, B, F).

At mid-latitudes (50–54°S), the Early Holocene thermal optimum reduced the thermal gradient, weakening winds at the northern margin of the SHW belt, as observed on Macquarie Island (54°S) (Saunders et al., 2018) (Fig. 7F) and on the leeward side of the Andes, where drier conditions were enhanced, indicated by higher non-arboreal pollen percentages (NAP) at Lake Cipreses in Patagonia (51°S) (Moreno et al., 2014) (Fig. 7A). Concurrently, the contraction of the SHW belt strengthened winds at higher latitudes, e.g. at Cape Horn (56°S), as indicated by abundant salinity-tolerant diatom taxa (Perren et al., 2025, Fig. 7B).

From 8000 to 3000 cal a BP (Fig. 8D and E), both our Kerguelen and Perren et al.'s Cape Horn temperature records (Fig. 7C and D) suggest a progressive poleward migration of the SHW. This is consistent with a reduction in the winter rainfall zones on the west coast of South Africa (Kirsten et al., 2020). On Amsterdam Island (37°S, 1400 km northeast of Kerguelen), Li et al. (2020) recorded a weakened and/or a northward SHW migration at 3900 cal a BP (Fig. 7E). Together with the Armor records, we conclude that the SHW migrated southward, leaving Amsterdam Island outside the belt and reducing wind intensity.

By contrast, two other periods (3000-2000 cal a BP, Figs. 8F, and 250 cal a BP-present, Fig. 8H) show a weaker positive SAM-*like* pattern: no major SST change was observed, suggesting that the SAF did not migrate as far south as during the Early Holocene (Figs. 7D and 8F–H). The most recent poleward SHW migration (250 cal a BP–present, Fig. 7C and 8H) was also recorded at Marion Island (46°S) (Perren et al., 2020).

In summary, as during the Mid and Late Holocene SST variations were less pronounced, whereas air temperature varied more, SHW latitudinal shifts were less marked. This suggests a predominance of atmospheric over oceanic processes in driving climate variability in the Kerguelen region during this period.

4.4.2. *Negative SAM-like periods*

We attribute the abrupt cooling between 9000 and 8000 cal a BP (Fig. 7D) to a northward migration of the APF towards the location of core MD11-3353, while the SAF shifted further north (Fig. 8C). At the same time, an air-mass reorganisation drastically reduced long-distance pollen transport to Kerguelen (Zwier et al., 2024) and cooled the atmosphere, favouring glaciers advance. This pattern coincides with increased sea-spray and stronger winds at Macquarie Island (Saunders et al., 2018, Fig. 7F) and reduced moisture in South Africa (Kirsten et al., 2020). In the South American sector, a similar northwards expansion of the SHW belt (i.e. negative SAM-like pattern) is suggested by windier conditions at mid-latitudes (50–54°S) (Fletcher and Moreno, 2012; McCulloch et al., 2023; Moreno et al., 2014; Spoth et al., 2023); Fig. 7A) and weaker winds at higher latitudes, such as Cape Horn (56°S) (Perren et al., 2025, Fig. 7B). However, this migration has occurred there later than in the Indian Ocean sector (7500 cal a BP vs. 9000 cal a BP).

Between 2000 and 250 cal a BP (Fig. 8G), our data exhibit a period of colder air temperature (Fig. 7C), *i.e.,* a negative SAM-*like* phase, consistent with local Kerguelen glacier dynamics (Charton et al., 2022). These interpretations are supported by records from the Indian Ocean which suggest a negative SAM-*like* period (Charton et al., 2022; Li et al., 2020; Perren et al., 2020; Van Der Putten et al., 2008; Zwier et al., 2024), South America (Fletcher and Moreno, 2012; McCulloch et al., 2023; Moreno et al., 2021; Spoth et al., 2023; van der Bilt et al., 2017, 2022; Xia et al., 2020), and South Africa (Kirsten et al., 2020).

However, the Mid and Late Holocene shows greater disparities around the world in terms of SHW migration than the Early Holocene (Fletcher and Moreno, 2012). In the Southern Hemisphere, the air temperature may also be influenced by other factors, like volcanic activity and other climatic modes (as El Niño Southern Oscillation). This may also reflect local changes and interactions between climatic modes. For example, more frequent El Niño events after ~6200 BP (Fletcher and Moreno, 2012; Moy et al., 2002) may have introduced a meridional component into this otherwise zonal pattern, possibly linked in the Indian Ocean to the Indian Ocean Dipole (IOD). To support this hypothesis, further studies should investigate potential teleconnections between the subantarctic and more tropical parts of the Southern Indian Ocean.

5. Conclusion

The lack of continental archives in the Southern Indian Ocean limits our knowledge about SHW dynamics over the Holocene. Based on our first continuous and quantitative reconstruction of air and sea surface temperatures for the Kerguelen region, we provide new insights and additional reference curves for palaeoclimate studies. By comparing those independent records, we reveal that the currently observed correlation between SST and air temperatures did not apply over longer timescales. One of the main discoveries of this study is converging evidence for a warm and potentially wet period between 4500 and 1500 cal a BP which, to our knowledge, had not been reported previously. Moreover, recent warming has rarely been observed, particularly in GDGT-inferred temperatures.

In inland areas in the Kerguelen region, the atmospheric system is decoupled from the oceanic system and is influenced primarily by fluctuations in the SHW belt location. Consequently, the air temperatures in the Kerguelen area vary independently of the SST. Caution is, therefore, required when using the SST as a proxy for air temperature,

notably in inland regions.

We report a major northward shift of the SHW belt at 9000 cal a BP as a consequence of a major global reorganisation of oceanic and atmospheric circulations, at least at the highest latitudes of the Southern Hemisphere.

Overall, the Mid- and Late-Holocene contraction/expansion patterns of the SHW belt explain the small changes in SST and the larger changes in air temperature without major air temperature changes without major reorganisations of oceanic fronts.

Use of artificial intelligence

We used artificialintelligence, ChatGPT (OpenAI, 2025), to improve the Englishgrammar and syntax of this manuscript.

Declaration of competing interest

The authors declare that they have no known competing financial interests or personal relationships that could have appeared to influence the work reported in this paper.

Acknowledgements

We are deeply grateful to the LEFE-IMAGO (Fluid Envelopes and the Environment – Multiple Interactions in the Atmosphere, Ice, and Ocean) research program of the CNRS, which has funded our analysis within the COUAC (Coupled Ocean–Atmosphere Climatic Processes in the Subantarctic Indian Ocean throughout the Holocene) project. We are warmly grateful to IPEV, the French Polar Institute, for providing necessary logistical support for field expeditions (programmes 448-PEISACG, 444-DyLIOKer, and 1094-PALAS). Roland Pagni and Dries Boone are warmly thanked for their help in the field. The authors thank the French CNRS-INSU national coring facility and, in particular the ANR-11 EQPX-0009-CLIMCOR project, for providing coring facilities. Radiocarbon dating referred to as SacA was performed at the LMC14 facility in Saclay, within the framework of the national programme ARTEMIS. The authors express their grateful thanks to the LMC14 team, particularly to Jean-Pascal Dumoulin, as well as to Tomas Goslar from Poznan Radiocarbon Laboratory for constant help in the management of ^{14}C samples and results. XRF core scanning was performed thanks at EDYTEM laboratory as part of the CEMBRO regional analytical facility. The authors thank the Laboratoire Souterrain de Modane (LSM) facilities for the gamma spectrometry measurements and Environnement, Dynamique et Territories de Montagne (EDYTEM) for short-lived radionuclide measurements. The Norwegian contribution was funded by the Norwegian Research Council under the project Shifting Climate States of the Polar Regions (SHIFTS) (project number; 210004).

Emeline Bellet benefited from a PhD grant from the École Doctorale Sciences de l'Ingénierie et de l'Environnement. This manuscript was greatly improved thanks to the constructive comments of three anonymous reviewers. Patrick Riaoul, editor at QSR, is acknowledged for his help and constructive comments throughout the review process.

We gratefully thank Ingrig Antheaume, who was a research engineer, without whom the ^{13}C and D/H measurements of *n*-alkanes on sediment from ARM14-I would not have been possible in Lyon.

We thank Cécile Pignol, engineer at Edytem, a lot for her help in publishing the data in the Data. indores data repository.

We thank Marjorie Fis and Anouk Leloup Besson, who worked on Armor sediment cores during their master's internship. Finally, Emeline Bellet expresses her sincere gratitude to William Rapuc and Julia Garagnon for their support and advice on this first paper.

Appendix A. Supplementary data

Supplementary data to this article can be found online at https://doi.org/10.1016/j.quascirev.2025.109753.

Data availability

https://doi.org/10.48579/PRO/LDHE9I

References

Abram, N.J., Mulvaney, R., Vimeux, F., Phipps, S.J., Turner, J., England, M.H., 2014. Evolution of the Southern Annular Mode during the past millennium. Nat. Clim. Change 4 (7), 564–569. https://doi.org/10.1038/nclimate2235.

Ai, X.E., Thöle, L.M., Auderset, A., Schmitt, M., Moretti, S., Studer, A.S., Michel, E., Wegmann, M., Mazaud, A., Bijl, P.K., Sigman, D.M., Martínez-García, A., Jaccard, S. L., 2024. The southward migration of the Antarctic Circumpolar Current enhanced oceanic degassing of carbon dioxide during the last two deglaciations. Commun. Earth Environ. 5 (1), 1–12. https://doi.org/10.1038/s43247-024-01216-x.

Aichner, B., Herzschuh, U., Wilkes, H., Vieth, A., Böhner, J., 2010. δD values of n-alkanes in Tibetan lake sediments and aquatic macrophytes – a surface sediment study and application to a 16ka record from Lake Koucha. Org. Geochem. 41 (8), 779–790. https://doi.org/10.1016/j.orggeochem.2010.05.010.

Allison, L.C., Johnson, H.L., Marshall, D.P., Munday, D.R., 2010. Where do winds drive the Antarctic Circumpolar Current? Geophys. Res. Lett. 37 (12). https://doi.org/10.1029/2010GL043355 n/a-n/a.

Arnaud, F., Sabatier, P., Leloup, A., Servettaz, A., Moine, B., Develle, A.-L., Guédron, S., Perrot, V., Pignol, C., Poulenard, J., 2020. In: Holocene tephrochronology of Kerguelen Archipelago, Subantarctic Indian Ocean. https://eartharxiv.org/repository/view/286/.

Bauersachs, T., Schubert, C.J., Mayr, C., Gilli, A., Schwark, L., 2024. Branched GDGT-based temperature calibrations from Central European Lakes. Sci. Total Environ. 906, 167724. https://doi.org/10.1016/j.scitotenv.2023.167724.

Berger, André L., 1978. Long-Term Variations of Daily Insolation and Quaternary Climatic Changes. J. Atmos. Sci 35 (12), 2362–2367. https://doi.org/10.1175/1520-0469(1978)035%253C2362:LTVODI%253E2.0.CO;2.

Bianchi, C., Gersonde, R., 2004. Climate evolution at the last deglaciation: the role of the Southern Ocean. Earth Planet Sci. Lett. 228 (3), 407–424. https://doi.org/10.1016/j.epsl.2004.10.003.

Blaauw, M., Christen, J.A., 2011. Flexible paleoclimate age-depth models using an autoregressive gamma process. Bayes. Anal. 6 (3), 457–474. https://doi.org/10.1214/11-BA618.

Blaga, C.I., Reichart, G.-J., Schouten, S., Lotter, A.F., Werne, J.P., Kosten, S., Mazzeo, N., Lacerot, G., Sinninghe Damsté, J.S., 2010. Branched glycerol dialkyl glycerol tetraethers in lake sediments: can they be used as temperature and pH proxies? Org. Geochem. 41 (11), 1225–1234. https://doi.org/10.1016/j.orggeochem.2010.07.002.

Castañeda, I.S., Schouten, S., 2011. A review of molecular organic proxies for examining modern and ancient lacustrine environments. Quat. Sci. Rev. 30 (21), 2851–2891. https://doi.org/10.1016/j.quascirev.2011.07.009.

Charton, J., Jomelli, V., Schimmelpfennig, I., Verfaillie, D., Favier, V., Mokadem, F., Gilbert, A., Brun, F., Aumaître, G., Bourlès, D.L., Keddadouche, K., 2021. A debris-covered glacier at Kerguelen (49°S, 69°E) over the past 15 000 years. Antarct. Sci. 33 (1), 103–115. https://doi.org/10.1017/S0954102020000541.

Charton, J., Schimmelpfennig, I., Jomelli, V., Delpech, G., Blard, P.-H., Braucher, R., Verfaillie, D., Favier, V., Rinterknecht, V., Goosse, H., Crosta, X., Chassiot, L., Martin, L., Guillaume, D., Legentil, C., 2022. New cosmogenic nuclide constraints on Late Glacial and Holocene glacier fluctuations in the sub-Antarctic Indian Ocean (Kerguelen Islands, 49°S). Quat. Sci. Rev. 283, 107461. https://doi.org/10.1016/j.quascirev.2022.107461.

Chassiot, L., Chapron, E., Michel, E., Jomelli, V., Favier, V., Verfaillie, D., Foucher, A., Charton, J., Paterne, M., Van der Putten, N., 2024. Late Holocene record of subantarctic glacier variability in Table Fjord, Cook Ice Cap, Kerguelen Islands. Quat. Sci. Rev. 344, 108980. https://doi.org/10.1016/j.quascirev.2024.108980.

Chaudhuri, P., Marron, J.S., 1999. SiZer for exploration of structures in curves. J. Am. Stat. Assoc. 94 (447), 807–823. https://doi.org/10.1080/01621459.1999.10474186.

Ciais, P., Jouzel, J., Petit, J.R., Lipenkov, V., White, J.W.C., 1994. Holocene temperature variations inferred from Antarctic ice cores. Ann. Glaciol. 20, 427–436. https://doi.org/10.3189/1994AoG20-1-427-436.

Civel-Mazens, M., Crosta, X., Cortese, G., Michel, E., Mazaud, A., Ther, O., Ikehara, M., Itaki, T., 2021a. Antarctic Polar Front migrations in the Kerguelen Plateau region, Southern Ocean, over the past 360 kyrs. Global Planet. Change 202, 103526. https://doi.org/10.1016/j.gloplacha.2021.103526.

Civel-Mazens, M., Crosta, X., Cortese, G., Michel, E., Mazaud, A., Ther, O., Ikehara, M., Itaki, T., 2021b. Impact of the Agulhas return current on the oceanography of the Kerguelen Plateau region, Southern Ocean, over the last 40 kyrs. Quat. Sci. Rev. 251, 106711. https://doi.org/10.1016/j.quascirev.2020.106711.

Crosta, X., Koç, N., 2007. Chapter eight diatoms: from micropaleontology to isotope geochemistry. In: Hillaire–Marcel, C., De Vernal, A. (Eds.), Developments in Marine Geology, vol. 1. Elsevier, pp. 327–369. https://doi.org/10.1016/S1572-5480(07)01013-5.

Crosta, X., Shukla, S.K., Ther, O., Ikehara, M., Yamane, M., Yokoyama, Y., 2020. Last Abundant Appearance Datum of *Hemidiscus karstenii* driven by climate change. Mar. Micropaleontol. 157, 101861. https://doi.org/10.1016/j.marmicro.2020.101861.

De Deckker, P., 2022. The Holocene hypsithermal in the Australian region. Quater. Sci. Adv. 7, 100061. https://doi.org/10.1016/j.qsa.2022.100061.

De Jonge, C., Hopmans, E.C., Zell, C.I., Kim, J.-H., Schouten, S., Sinninghe Damsté, J.S., 2014a. Occurrence and abundance of 6-methyl branched glycerol dialkyl glycerol

tetraethers in soils: implications for palaeoclimate reconstruction. Geochem. Cosmochim. Acta 141, 97–112. https://doi.org/10.1016/j.gca.2014.06.013.
De Jonge, C., Hopmans, E.C., Zell, C.I., Kim, J.-H., Schouten, S., Sinninghe Damsté, J.S., 2014b. Occurrence and abundance of 6-methyl branched glycerol dialkyl glycerol tetraethers in soils: implications for palaeoclimate reconstruction. Geochem. Cosmochim. Acta 141, 97–112. https://doi.org/10.1016/j.gca.2014.06.013.
Dumoulin, J.-P., Comby-Zerbino, C., Delqué-Količ, E., Moreau, C., Caffy, I., Hain, S., Perron, M., Thellier, B., Setti, V., Berthier, B., Beck, L., 2017. Status report on sample preparation protocols developed at the LMC14 laboratory, saclay, France: from sample collection to 14C AMS measurement. Radiocarbon 59 (3), 713–726. https://doi.org/10.1017/RDC.2016.116.
Eglinton, T.I., Aluwihare, L.I., Bauer, J.E., Druffel, E.R., McNichol, A.P., 1996. Gas chromatographic isolation of individual compounds from complex matrices for radiocarbon dating. Anal. Chem. 68 (5), 904–912. https://doi.org/10.1021/ac9508513.
Erb, M.P., McKay, N.P., Steiger, N., Dee, S., Hancock, C., Ivanovic, R.F., Gregoire, L.J., Valdes, P., 2022. Reconstructing Holocene temperatures in time and space using paleoclimate data assimilation. Clim. Past 18 (12), 2599–2629. https://doi.org/10.5194/cp-18-2599-2022.
Favier, V., Verfaillie, D., Berthier, E., Menegoz, M., Jomelli, V., Kay, J.E., Ducret, L., Malbéteau, Y., Brunstein, D., Gallée, H., Park, Y.-H., Rinterknecht, V., 2016a. Atmospheric drying as the main driver of dramatic glacier wastage in the southern Indian Ocean. Sci. Rep. 6, 32396. https://doi.org/10.1038/srep32396.
Favier, V., Verfaillie, D., Berthier, E., Menegoz, M., Jomelli, V., Kay, J.E., Ducret, L., Malbéteau, Y., Brunstein, D., Gallée, H., Park, Y.-H., Rinterknecht, V., 2016b. Atmospheric drying as the main driver of dramatic glacier wastage in the southern Indian Ocean. Sci. Rep. 6 (1), 32396. https://doi.org/10.1038/srep32396.
Ficken, K.J., Li, B., Swain, D.L., Eglinton, G., 2000. An *n*-alkane proxy for the sedimentary input of submerged/floating freshwater aquatic macrophytes. Org. Geochem. 31 (7), 745–749. https://doi.org/10.1016/S0146-6380(00)00081-4.
Fletcher, M.-S., Moreno, P.I., 2012. Have the Southern Westerlies changed in a zonally symmetric manner over the last 14,000 years? A hemisphere-wide take on a controversial problem. Quat. Int. 253, 32–46. https://doi.org/10.1016/j.quaint.2011.04.042.
Fogt, R.L., Marshall, G.J., 2020a. The Southern annular mode: variability, trends, and climate impacts across the Southern Hemisphere. WIREs Clim. Change 11 (4), e652. https://doi.org/10.1002/wcc.652.
Fogt, R.L., Marshall, G.J., 2020b. The Southern annular mode: variability, trends, and climate impacts across the Southern Hemisphere. WIREs Clim. Change 11 (4), e652. https://doi.org/10.1002/wcc.652.
Forster, P.M., Maycock, A.C., McKenna, C.M., Smith, C.J., 2020. Latest climate models confirm need for urgent mitigation. Nat. Clim. Change 10 (1). https://doi.org/10.1038/s41558-019-0660-0. Article 1.
Foster, L.C., Pearson, E.J., Juggins, S., Hodgson, D.A., Saunders, K.M., Verleyen, E., Roberts, S.J., 2016. Development of a regional glycerol dialkyl glycerol tetraether (GDGT)–temperature calibration for Antarctic and sub-Antarctic lakes. Earth Planet Sci. Lett. 433, 370–379. https://doi.org/10.1016/j.epsl.2015.11.018.
Frenot, Y., Gloaguen, J.C., Massé, L., Lebouvier, M., 2001. Human activities, ecosystem disturbance and plant invasions in subantarctic Crozet, Kerguelen and Amsterdam Islands. Biol. Conserv. 101 (1), 33–50. https://doi.org/10.1016/S0006-3207(01)00052-0.
Frenot, Y., Gloaguen, J.-C., Van De Vijver, B., Beyens, L., 1997. Datation de quelques sédiments tourbeux holocènes et oscillations glaciaires aux îles Kerguelen. Compt. Rendus Acad. Sci. III Sci. Vie. 320 (7), 567–573. https://doi.org/10.1016/S0764-4469(97)84712-9.
Gillett, N.P., Fyfe, J.C., 2013. Annular mode changes in the CMIP5 simulations. Geophys. Res. Lett. 40 (6), 1189–1193. https://doi.org/10.1002/grl.50249.
Gillett, N.P., Kell, T.D., Jones, P.D., 2006. Regional climate impacts of the Southern Annular Mode. Geophys. Res. Lett. 33 (23). https://doi.org/10.1029/2006GL027721.
Gilli, A., Ariztegui, D., Anselmetti, F.S., McKenzie, J.A., Markgraf, V., Hajdas, I., McCulloch, R.D., 2005. Mid-Holocene strengthening of the Southern Westerlies in South America—Sedimentological evidences from Lago Cardiel, Argentina (49°S). Global Planet. Change 49 (1–2), 75–93. https://doi.org/10.1016/j.gloplacha.2005.05.004.
Gottschalk, J., Michel, E., Thöle, L.M., Studer, A.S., Hasenfratz, A.P., Schmid, N., Butzin, M., Mazaud, A., Martínez-García, A., Szidat, S., Jaccard, S.L., 2020. Glacial heterogeneity in Southern Ocean carbon storage abated by fast South Indian deglacial carbon release. Nat. Commun. 11 (1), 6192. https://doi.org/10.1038/s41467-020-20034-1.
Guiot, J., de Vernal, A., 2011. Is spatial autocorrelation introducing biases in the apparent accuracy of paleoclimatic reconstructions? Quat. Sci. Rev. 30 (15), 1965–1972. https://doi.org/10.1016/j.quascirev.2011.04.022.
Heaton, T.J., Köhler, P., Butzin, M., Bard, E., Reimer, R.W., Austin, W.E.N., Ramsey, C.B., Grootes, P.M., Hughen, K.A., Kromer, B., Reimer, P.J., Adkins, J., Burke, A., Cook, M. S., Olsen, J., Skinner, L.C., 2020. Marine20—The marine radiocarbon Age calibration curve (0–55,000 cal BP). Radiocarbon 62 (4), 779–820. https://doi.org/10.1017/RDC.2020.68.
Heirman, K., De Batist, M., Arnaud, F., De Beaulieu, J.-L., 2012. Seismic stratigraphy of the late Quaternary sedimentary infill of Lac d'Armor (Kerguelen archipelago): a record of glacier retreat, sedimentary mass wasting and southern Westerly intensification. Antarct. Sci. 24 (6), 608–618. https://doi.org/10.1017/S0954102012000466.
Hersbach, H., Bell, W., Berrisford, P., Horányi, A.J.M.-S., Nicolas, J., Radu, R., Schepers, D., Simmons, A., Soci, C., Dee, D., 2019. Global reanalysis: goodbye ERA-Interim, hello ERA5. https://doi.org/10.21957/VF291HEHD7.
Hogg, Alan, G., Heaton, Timothy J., Quan Hua, et al., 2020. SHCal20 Southern Hemisphere Calibration, 0–55,000 Years Cal BP. Radiocarbon 62 (4), 759–778. https://doi.org/10.1017/RDC.2020.59.
Hopmans, E.C., Schouten, S., Sinninghe Damsté, J.S., 2016. The effect of improved chromatography on GDGT-based palaeoproxies. Org. Geochem. 93, 1–6. https://doi.org/10.1016/j.orggeochem.2015.12.006.
Huang, X., Xue, J., Wang, X., Meyers, P., 2015. Environmental controls on leaf wax δD ratios in surface peats across the monsoonal region of China. Biogeosci. Discuss. 12, 15157–15184. https://doi.org/10.5194/bgd-12-15157-2015.
Huguet, C., Hopmans, E.C., Febo-Ayala, W., Thompson, D.H., Sinninghe Damsté, J.S., Schouten, S., 2006. An improved method to determine the absolute abundance of glycerol dibiphytanyl glycerol tetraether lipids. Org. Geochem. 37 (9). https://doi.org/10.1016/j.orggeochem.2006.05.008. Article 9.
Ingolfsson, O., Hjort, C., Humlum, O., 2003. Glacial and climate history of the antarctic peninsula since the last glacial maximum. Arctic Antarct. Alpine Res. 35 (2), 175–186.
Jacob, J., Huang, Y., Disnar, J.-R., Sifeddine, A., Boussafir, M., Spadano Albuquerque, A. L., Turcq, B., 2007. Paleohydrological changes during the last deglaciation in Northern Brazil. Quat. Sci. Rev. 26 (7), 1004–1015. https://doi.org/10.1016/j.quascirev.2006.12.004.
Jomelli, V., Charton, J., Schimmelpfennig, I., Verfaillie, D., Favier, V., Mokadem, F., Gilbert, A., Brun, F., Aumaître, G., Bourlès, D.L., Keddadouche, K., 2021. Evolution of a debris-covered glacier in the Kerguelen Archipelago (49°S, 69°E) over the past 15,000 years constrained by in situ cosmogenic 36Cl dating. EGU21-13304. EGU General Assembly Conference Abstracts. https://doi.org/10.5194/egusphere-egu21-13304.
Jones, Julie, M., Fogt, Ryan L., Martin Widmann, Marshall, Gareth J., Jones, Phil D., Martin Visbeck, 2009. Historical SAM Variability. Part I: Century-Length Seasonal Reconstructions*. J. Climate 22 (20), 5319–5345. https://doi.org/10.1175/2009JCLI2785.1.
Jomelli, V., Mokadem, F., Schimmelpfennig, I., Chapron, E., Rinterknecht, V., Favier, V., Verfaillie, D., Brunstein, D., Legentil, C., Michel, E., Swingedouw, D., Jaouen, A., Aumaitre, G., Bourlès, D.L., Keddadouche, K., 2017. Sub-Antarctic glacier extensions in the Kerguelen region (49°S, Indian Ocean) over the past 24,000 years constrained by 36Cl moraine dating. Quat. Sci. Rev. 162, 128–144. https://doi.org/10.1016/j.quascirev.2017.03.010.
Jomelli, V., Schimmelpfennig, I., Favier, V., Mokadem, F., Landais, A., Rinterknecht, V., Brunstein, D., Verfaillie, D., Legentil, C., Aumaitre, G., Bourlès, D.L., Keddadouche, K., 2018. Glacier extent in sub-Antarctic Kerguelen archipelago from MIS 3 period: evidence from 36Cl dating. Quat. Sci. Rev. 183, 110–123. https://doi.org/10.1016/j.quascirev.2018.01.008.
Kim, J.-H., Crosta, X., Michel, E., Schouten, S., Duprat, J., Damsté, J.S.S., 2009. Impact of lateral transport on organic proxies in the Southern Ocean. Quat. Res. 71 (2), 246–250. https://doi.org/10.1016/j.yqres.2008.10.005.
Kim, J.-H., Zell, C., Moreira-Turcq, P., Pérez, M.A.P., Abril, G., Mortillaro, J.-M., Weijers, J.W.H., Meziane, T., Sinninghe Damsté, J.S., 2012. Tracing soil organic carbon in the lower Amazon River and its tributaries using GDGT distributions and bulk organic matter properties. Geochem. Cosmochim. Acta 90, 163–180. https://doi.org/10.1016/j.gca.2012.05.014.
Kirsten, K.L., Kasper, T., Cawthra, H.C., Strobel, P., Quick, L.J., Meadows, M.E., Haberzettl, T., 2020. Holocene variability in climate and oceanic conditions in the winter rainfall zone of South Africa—inferred from a high resolution diatom record from Verlorenvlei. J. Quat. Sci. 35 (4), 572–581. https://doi.org/10.1002/jqs.3200.
Knutti, R., Rugenstein, M.A.A., Hegerl, G.C., 2017. Beyond equilibrium climate sensitivity. Nat. Geosci. 10 (10). https://doi.org/10.1038/ngeo3017. Article 10.
Labracherie, M., Labeyrie, L.D., Duprat, J., Bard, E., Arnold, M., Pichon, J.-J., Duplessy, J.-C., 1989. The last deglaciation in the Southern Ocean. Paleoceanography 4 (6), 629–638. https://doi.org/10.1029/PA004i006p00629.
Lamy, F., Hebbeln, D., Röhl, U., Wefer, G., 2001. Holocene rainfall variability in southern Chile: a marine record of latitudinal shifts of the Southern Westerlies. Earth Planet Sci. Lett. 185 (3), 369–382. https://doi.org/10.1016/S0012-821X(00)00381-2.
Lamy, F., Kilian, R., Arz, H.W., Francois, J.-P., Kaiser, J., Prange, M., Steinke, T., 2010. Holocene changes in the position and intensity of the southern westerly wind belt. Nat. Geosci. 3 (10). https://doi.org/10.1038/ngeo959. Article 10.
Li, C., Sonke, J.E., Le Roux, G., Van der Putten, N., Piotrowska, N., Jeandel, C., Mattielli, N., Benoit, M., Wiggs, G.F.S., De Vleeschouwer, F., 2020. Holocene dynamics of the southern westerly winds over the Indian Ocean inferred from a peat dust deposition record. Quat. Sci. Rev. 231, 106169. https://doi.org/10.1016/j.quascirev.2020.106169.
Liu, J., An, Z., Liu, H., 2018. Leaf wax n-alkane distributions across plant types in the central Chinese Loess Plateau. Org. Geochem. 125, 260–269. https://doi.org/10.1016/j.orggeochem.2018.09.006.
Locarnini, M., Mishonov, A., Baranova, O., Boyer, T., Zweng, M., Garcia, H., Reagan, J., Seidov, D., Weathers, K., Paver, C., Smolyar, I., Baranova, O., Boyer, T., Zweng, M., Garcia, H., Reagan, J., Seidov, D., Weathers, K., Paver, C., Smolyar, I., 2018. World Ocean Atlas 2018. Temperature (Austin) 1. https://archimer.ifremer.fr/doc/00651/76338/.
Marshall, G.J., 2003. Trends in the Southern annular mode from observations and reanalyses. J. Clim. 16 (24), 4134–4143. https://doi.org/10.1175/1520-0442(2003)016%253C4134:TITSAM%253E2.0.CO, 2.
Marshall, G.J., 2007. Half-century seasonal relationships between the Southern Annular mode and Antarctic temperatures. Int. J. Climatol. 27 (3), 373–383. https://doi.org/10.1002/joc.1407.
Martínez-Sosa, P., Tierney, J.E., Stefanescu, I.C., Dearing Crampton-Flood, E., Shuman, B.N., Routson, C., 2021. A global Bayesian temperature calibration for

lacustrine brGDGTs. Geochem. Cosmochim. Acta 305, 87–105. https://doi.org/10.1016/j.gca.2021.04.038.
Mazaud, A., Michel, E., 2011. MD 185/INDIEN SUD 1 cruise,Marion Dufresne R/V. Sismer. https://doi.org/10.17600/11200030.
McCulloch, R.D., Mansilla, C.A., Roberts, S.J., Tisdall, E.W., 2023. Late Quaternary climatic inferences from southern Patagonia (~53°S): a holistic palaeoecological approach to tracking the behaviour of the southern westerly winds. Palaeogeogr. Palaeoclimatol. Palaeoecol. 631, 111822. https://doi.org/10.1016/j.palaeo.2023.111822.
McGlone, M.S., Turney, C.S.M., Wilmshurst, J.M., Renwick, J., Pahnke, K., 2010. Divergent trends in land and ocean temperature in the Southern Ocean over the past 18,000 years. Nat. Geosci. 3 (9), 622–626. https://doi.org/10.1038/ngeo931.
McGlone, M.S., Wilmshurst, J.M., Richardson, S.J., Turney, C.S.M., Wood, J.R., 2019. Temperature, wind, cloud, and the postglacial tree line history of sub-Antarctic Campbell Island. Forests 10 (11), 998. https://doi.org/10.3390/f10110998.
Moreau, C., Messager, C., Berthier, B., Hain, S., Thellier, B., Dumoulin, J.-P., Caffy, I., Sieudat, M., Delqué-Količ, E., Mussard, S., Perron, M., Setti, V., Beck, L., 2020. Artemis, the 14c ams facility of the lmc14 national laboratory: a status report on quality control and microsample procedures. Radiocarbon 62 (6), 1755–1770. https://doi.org/10.1017/RDC.2020.73.
Moreno, P.I., Francois, J.P., Moy, C.M., Villa-Martínez, R., 2010. Covariability of the Southern Westerlies and atmospheric CO2 during the Holocene. Geology 38 (8), 727–730. https://doi.org/10.1130/G30962.1.
Moreno, P.I., Henríquez, W.I., Pesce, O.H., Henríquez, C.A., Fletcher, M.S., Garreaud, R. D., Villa-Martínez, R.P., 2021. An early Holocene westerly minimum in the southern mid-latitudes. Quat. Sci. Rev. 251, 106730. https://doi.org/10.1016/j.quascirev.2020.106730.
Moreno, P.I., Vilanova, I., Villa-Martínez, R., Dunbar, R.B., Mucciarone, D.A., Kaplan, M. R., Garreaud, R.D., Rojas, M., Moy, C.M., De Pol-Holz, R., Lambert, F., 2018. Onset and evolution of Southern annular mode-like changes at Centennial timescale. Sci. Rep. 8 (1). https://doi.org/10.1038/s41598-018-21836-6. Article 1.
Moreno, P.I., Vilanova, I., Villa-Martínez, R., Garreaud, R.D., Rojas, M., De Pol-Holz, R., 2014. Southern Annular mode-like changes in Southwestern Patagonia at Centennial timescales over the last three millennia. Nat. Commun. 5 (1), 4375. https://doi.org/10.1038/ncomms5375.
Moy, C.M., Seltzer, G.O., Rodbell, D.T., Anderson, D.M., 2002. Variability of El Niño/Southern Oscillation activity at millennial timescales during the Holocene epoch. Nature 420 (6912), 162–165. https://doi.org/10.1038/nature01194.
Mulvaney, R., Abram, N.J., Hindmarsh, R.C.A., Arrowsmith, C., Fleet, L., Triest, J., Sime, L.C., Alemany, O., Foord, S., 2012. Recent Antarctic Peninsula warming relative to Holocene climate and ice-shelf history. Nature 489 (7414), 141–144. https://doi.org/10.1038/nature11391.
Nielsen, S.H.H., Koç, N., Crosta, X., 2004. Holocene climate in the Atlantic sector of the Southern Ocean: controlled by insolation or oceanic circulation? Geology 32 (4), 317–320. https://doi.org/10.1130/G20334.1. Scopus.
Ooms, M., Vijver, B.V., Temmerman, S., Beyens, L., 2011. A Holocene palaeoenviromental study of a sediment core from Ile de la Possession, Iles Crozet, sub-Antarctica. Antarct. Sci. 23 (5), 431–441. https://doi.org/10.1017/S0954102011000277.
Orme, L.C., Crosta, X., Miettinen, A., Divine, D.V., Husum, K., Isaksson, E., Wacker, L., Mohan, R., Ther, O., Ikehara, M., 2020. Sea surface temperature in the Indian sector of the Southern Ocean over the Late Glacial and Holocene. Clim. Past 16 (4), 1451–1467. https://doi.org/10.5194/cp-16-1451-2020.
Orsi, A.H., Whitworth, T., Nowlin, W.D., 1995. On the meridional extent and fronts of the Antarctic Circumpolar Current. Deep Sea Res. Oceanogr. Res. Pap. 42 (5), 641–673. https://doi.org/10.1016/0967-0637(95)00021-W.
Pahnke, K., Sachs, J.P., 2006. Sea surface temperatures of southern midlatitudes 0–160 kyr B.P. Paleoceanography 21 (2). https://doi.org/10.1029/2005PA001191, 2005PA001191.
Park, Y.-H., Park, T., Kim, T.-W., Lee, S.-H., Hong, C.-S., Lee, J.-H., Rio, M.-H., Pujol, M.-I., Ballarotta, M., Durand, I., Provost, C., 2019. Observations of the Antarctic Circumpolar Current over the udintsev fracture Zone, the narrowest Choke point in the Southern Ocean. J. Geophys. Res.: Oceans 124 (7), 4511–4528. https://doi.org/10.1029/2019JC015024.
Park, Y., Vivier, F., Roquet, F., Kestenare, E., 2009. Direct observations of the ACC transport across the Kerguelen Plateau. Geophys. Res. Lett. 36 (18). https://doi.org/10.1029/2009GL039617, 2009GL039617.
Paterne, M., Michel, E., Héros, V., 2019. Variability of marine 14C reservoir ages in the Southern Ocean highlighting circulation changes between 1910 and 1950. Earth Planet Sci. Lett. 511, 99–104. https://doi.org/10.1016/j.epsl.2019.01.029.
Pearson, E.J., Juggins, S., Talbot, H.M., Weckström, J., Rosén, P., Ryves, D.B., Roberts, S. J., Schmidt, R., 2011. A lacustrine GDGT-temperature calibration from the Scandinavian Arctic to Antarctic: renewed potential for the application of GDGT-paleothermometry in lakes. Geochem. Cosmochim. Acta 75 (20), 6225–6238. https://doi.org/10.1016/j.gca.2011.07.042.
Perren, B.B., Hodgson, D.A., Roberts, S.J., Sime, L., Van Nieuwenhuyze, W., Verleyen, E., Vyverman, W., 2020. Southward migration of the Southern Hemisphere westerly winds corresponds with warming climate over centennial timescales. Commun. Earth Environ. 1 (1). https://doi.org/10.1038/s43247-020-00059-6. Article 1.
Perren, B.B., Kaiser, J., Arz, H.W., Dellwig, O., Hodgson, D.A., Lamy, F., 2025. Poleward displacement of the Southern Hemisphere Westerlies in response to Early Holocene warming. Commun. Earth Environ. 6 (1), 164. https://doi.org/10.1038/s43247-025-02129-z.
Pohl, B., Saucède, T., Favier, V., Pergaud, J., Verfaillie, D., Féral, J.-P., Krasniqi, Y., Richard, Y., 2021. Recent climate variability around the kerguelen Islands (Southern Ocean) seen through weather regimes. J. Appl. Meteorol. Climatol. 60 (5), 711–731. https://doi.org/10.1175/JAMC-D-20-0255.1.
Poynter, J., Eglinton, G., 1990. Molecular composition of three sediments from hole 717C: the Bengal fan. In: Cochran, J.R., Stow, D.A.V., et al. (Eds.), Ocean Drill. Prog. 116. https://doi.org/10.2973/odp.proc.sr.116.1990.
Raberg, J.H., Harning, D.J., Crump, S.E., de Wet, G., Blumm, A., Kopf, S., Geirsdóttir, Á., Miller, G.H., Sepúlveda, J., 2021. Revised fractional abundances and warm-season temperatures substantially improve brGDGT calibrations in lake sediments. Biogeosciences 18 (12), 3579–3603. https://doi.org/10.5194/bg-18-3579-2021.
Rach, O., Kahmen, A., Brauer, A., and Sachse, D.: A dual-biomarker approach for quantification of changes in relative humidity from sedimentary lipid D/H ratios, Clim. Past, 13, 741–757, https://doi.org/10.5194/cp-13-741-2017.
Rao, Z., Zhu, Z., Wang, S., Jia, G., Qiang, M., Wu, Y., 2009. CPI values of terrestrial higher plant-derived long-chain n-alkanes: a potential paleoclimatic proxy. Front. Earth Sci. China 3 (3), 266–272. https://doi.org/10.1007/s11707-009-0037-1.
Razik, S., Chiessi, C.M., Romero, O.E., von Dobeneck, T., 2013. Interaction of the south American monsoon system and the Southern westerly wind belt during the last 14kyr. Palaeogeogr. Palaeoclimatol. Palaeoecol. 374, 28–40. https://doi.org/10.1016/j.palaeo.2012.12.022.
Reimer, Brown, Reimer, R., 2004. Discussion: reporting and calibration of post-bomb 14C data. Radiocarbon 46 (3), 1299–1304. https://doi.org/10.1017/S0033822200033154.
Rintoul, S.R., Church, J., Fahrbach, E., Garcia, M., Gordon, A., King, B., Morrow, R., Orsi, A.H., Speer, K., 2001. Monitoring and understanding Southern Ocean variability and its impact on climate: a strategy for sustained observations. In: Koblinsky, C.J., Smith, N.R. (Eds.), Observing the Oceans in the 21st Century. GODAE Project Office/Bureau of Meteorology, Melbourne, Australia, pp. 486–508.
Sabatier, P., Moernaut, J., Bertrand, S., Van Daele, M., Kremer, K., Chaumillon, E., Arnaud, F., 2022. A review of event deposits in Lake sediments. Quaternary 5 (3). https://doi.org/10.3390/quat5030034. Article 3.
Sachse, D., Billault, I., Bowen, G.J., Chikaraishi, Y., Dawson, T.E., Feakins, S.J., Freeman, K.H., Magill, C.R., McInerney, F.A., Van Der Meer, M.T.J., Polissar, P., Robins, R.J., Sachs, J.P., Schmidt, H.-L., Sessions, A.L., White, J.W.C., West, J.B., Kahmen, A., 2012. Molecular paleohydrology: interpreting the hydrogen-isotopic composition of lipid biomarkers from photosynthesizing organisms. Annu. Rev. Earth Planet Sci. 40 (1), 221–249. https://doi.org/10.1146/annurev-earth-042711-105535.
Saunders, K.M., Kamenik, C., Hodgson, D.A., Hunziker, S., Siffert, L., Fischer, D., Fujak, M., Gibson, J.A.E., Grosjean, M., 2012. Late Holocene changes in precipitation in northwest Tasmania and their potential links to shifts in the Southern Hemisphere westerly winds. Global Planet. Change 92–93, 82–91. https://doi.org/10.1016/j.gloplacha.2012.04.005.
Saunders, K.M., Roberts, S.J., Perren, B., Butz, C., Sime, L., Davies, S., Van Nieuwenhuyze, W., Grosjean, M., Hodgson, D.A., 2018. Holocene dynamics of the Southern Hemisphere westerly winds and possible links to CO2 outgassing. Nat. Geosci. 11 (9), 9. https://doi.org/10.1038/s41561-018-0186-5.
Schaaff, V., Grossi, V., Makou, M., Garcin, Y., Deschamps, P., Hamelin, B., Kiahtipes, C. A., Sebag, D., Ngounou Ngatcha, B., Ménot, G., 2025. Sensitivity to climate and vegetation dynamics of a peatland record from central Cameroon during the African Humid Period. Quat. Sci. Rev. 358, 109307. https://doi.org/10.1016/j.quascirev.2025.109307.
Schlitzer, R., 2002. Interactive analysis and visualization of geoscience data with Ocean Data View. Comput. Geosci. 28 (10), 1211–1218. https://doi.org/10.1016/S0098-3004(02)00040-7.
Shanahan, T.M., Hughen, K.A., Van Mooy, B.A.S., 2013. Temperature sensitivity of branched and isoprenoid GDGTs in Arctic Lakes. Org. Geochem. 64, 119–128. https://doi.org/10.1016/j.orggeochem.2013.09.010.
Siani, G., Michel, E., De Pol-Holz, R., DeVries, T., Lamy, F., Carel, M., Isguder, G., Dewilde, F., Lourantou, A., 2013. Carbon isotope records reveal precise timing of enhanced Southern Ocean upwelling during the last deglaciation. Nat. Commun. 4 (1), 2758. https://doi.org/10.1038/ncomms3758.
Sijp, W.P., England, M.H., 2008. The effect of a northward shift in the southern hemisphere westerlies on the global ocean. Prog. Oceanogr. 79 (1), 1–19. https://doi.org/10.1016/j.pocean.2008.07.002.
Simms, A.R., Ivins, E.R., DeWitt, R., Kouremenos, P., Simkins, L.M., 2012. Timing of the most recent Neoglacial advance and retreat in the South Shetland Islands, Antarctic Peninsula: insights from raised beaches and Holocene uplift rates. Quat. Sci. Rev. 47, 41–55. https://doi.org/10.1016/j.quascirev.2012.05.013.
Sleire, J.B., Bakke, J., Arnaud, F., Sabatier, P., Van Der Bilt, W.G.M., 2025. Multiple late Holocene glacier advances on the sub-Antarctic Kerguelen (49°S) islands: evidence from a 1200 yr sediment core from a glacial threshold basin. Quat. Sci. Rev. 347, 109106. https://doi.org/10.1016/j.quascirev.2024.109106.
Sokolov, S., Rintoul, S.R., 2009. Circumpolar structure and distribution of the Antarctic Circumpolar current fronts: 1. Mean circumpolar paths. J. Geophys. Res.: Oceans 114 (C11). https://doi.org/10.1029/2008JC005108, 2008JC005108.
Spoth, M., Hall, B., Lowell, T., Diefendorf, A.F., Corcoran, M.C., Brickle, P., 2023. Tracking the southern hemisphere westerlies during and since the last glacial maximum with multiproxy lake records from the Falkland Islands (52 °S). Quat. Sci. Rev. 311, 108135. https://doi.org/10.1016/j.quascirev.2023.108135.
Stenni, B., Masson-Delmotte, V., Johnsen, S., Jouzel, J., Longinelli, A., Monnin, E., Röthlisberger, R., Selmo, E., 2001. An Oceanic cold reversal during the last deglaciation. Science 293 (5537), 2074–2077. https://doi.org/10.1126/science.1059702.
Stenni, B., Masson-Delmotte, V., Selmo, E., Oerter, H., Meyer, H., Röthlisberger, R., Jouzel, J., Cattani, O., Falourd, S., Fischer, H., Hoffmann, G., Iacumin, P., Johnsen, S. J., Minster, B., Udisti, R., 2010. The deuterium excess records of EPICA Dome C and

Dronning Maud Land ice cores (East Antarctica). Quat. Sci. Rev. 29 (1), 146–159. https://doi.org/10.1016/j.quascirev.2009.10.009.
Sterken, M., Roberts, S.J., Hodgson, D.A., Vyverman, W., Balbo, A.L., Sabbe, K., Moreton, S.G., Verleyen, E., 2012. Holocene glacial and climate history of Prince Gustav Channel, northeastern Antarctic Peninsula. Quat. Sci. Rev. 31, 93–111. https://doi.org/10.1016/j.quascirev.2011.10.017.
Sun, Q., Chu, G., Liu, M., Xie, M., Li, S., Ling, Y., Wang, X., Shi, L., Jia, G., Lü, H., 2011. Distributions and temperature dependence of branched glycerol dialkyl glycerol tetraethers in recent lacustrine sediments from China and Nepal. J. Geophys. Res.: Biogeosciences 116 (G1). https://doi.org/10.1029/2010JG001365.
Sun, X., Zhao, C., Zhang, C., Feng, X., Yan, T., Yang, X., Shen, J., 2021. Seasonality in Holocene temperature reconstructions in Southwestern China. Paleoceanogr. Paleoclimatol. 36 (1). https://doi.org/10.1029/2020PA004025 e2020PA004025.
Swart, N.C., Fyfe, J.C., Gillett, N., Marshall, G.J., 2015. Comparing trends in the Southern annular mode and surface westerly jet. J. Clim. 28 (22), 8840–8859. https://doi.org/10.1175/JCLI-D-15-0334.1.
Thöle, L.M., Amsler, H.E., Moretti, S., Auderset, A., Gilgannon, J., Lippold, J., Vogel, H., Crosta, X., Mazaud, A., Michel, E., Martínez-García, A., Jaccard, S.L., 2019. Glacial-interglacial dust and export production records from the Southern Indian Ocean. Earth Planet Sci. Lett. 525, 115716. https://doi.org/10.1016/j.epsl.2019.115716.
Thompson, D.W.J., Wallace, J.M., 2000. Annular modes in the extratropical circulation. Part I: Month-to-month variability. J. Clim. 13, 1000–1016. https://doi.org/10.1175/1520-0442(2000)01360;1000:amitec62;2.0.co;2.
Toggweiler, J.R., 2009. Shifting westerlies. Science 323 (5920), 1434–1435. https://doi.org/10.1126/science.1169823.
Toggweiler, J.R., Russell, J.L., Carson, S.R., 2006. Midlatitude westerlies, atmospheric CO2, and climate change during the ice ages. Paleoceanography 21 (2). https://doi.org/10.1029/2005PA001154.
Totten, R.L., Anderson, J.B., Fernandez, R., Wellner, J.S., 2015. Marine record of Holocene climate, ocean, and cryosphere interactions: Herbert Sound, James Ross Island, Antarctica. Quat. Sci. Rev. 129, 239–259. https://doi.org/10.1016/j.quascirev.2015.09.009.
Tuestad, T., Marrero, S.M., Linge, H., Deline, P., Ravanel, L., Bakke, J., Arnaud, F., Hein, A.S., Gheorghiu, D.M., Shanks, R., 2024. Late Glacial-Holocene cirque glacier chronology on sub-Antarctic Kerguelen Archipelago (49°S) based on cosmogenic 36Cl exposure dating. Quat. Sci. Rev. 336, 108754. https://doi.org/10.1016/j.quascirev.2024.108754.
Van der Bilt, W.G.M., Bakke, J., Werner, J.P., Paasche, Ø., Rosqvist, G., Vatle, S.S., 2017. Late Holocene glacier reconstruction reveals retreat behind present limits and two-stage Little Ice Age on Subantarctic South Georgia. J. Quat. Sci. 32 (6), 888–901. https://doi.org/10.1002/jqs.2937.
Van der Bilt, W.G.M., D'Andrea, W.J., Oppedal, L.T., Bakke, J., Bjune, A.E., Zwier, M., 2022. Stable Southern Hemisphere westerly winds throughout the Holocene until intensification in the last two millennia. Commun. Earth Environ. 3 (1), 186. https://doi.org/10.1038/s43247-022-00512-8.
Van der Putten, N., Hébrard, J.-P., Verbruggen, C., Van de Vijver, B., Disnar, J.-R., Spassov, S., de Beaulieu, J.-L., De Dapper, M., Keravis, D., Hus, J., Thouveny, N., Frenot, Y., 2008. An integrated palaeoenvironmental investigation of a 6200 year old peat sequence from Ile de la Possession, Iles Crozet, sub-Antarctica. Palaeogeogr. Palaeoclimatol. Palaeoecol. 270 (1), 179–195. https://doi.org/10.1016/j.palaeo.2008.09.014.
Van Der Putten, N., Mauquoy, D., Verbruggen, C., Björck, S., 2012. Subantarctic peatlands and their potential as palaeoenvironmental and palaeoclimatic archives. Quat. Int. 268, 65–76. https://doi.org/10.1016/j.quaint.2011.07.032.
Van Der Putten, N., Stieperaere, H., Verbruggen, C., Ochyra, R., 2004. Holocene palaeoecology and climate history of South Georgia (sub-Antarctica) based on a macrofossil record of bryophytes and seeds. Holocene 14 (3), 382–392. https://doi.org/10.1191/0959683604hl714rp.
Van der Putten, N., Verbruggen, C., Björck, S., Michel, E., Disnar, J.-R., Chapron, E., Moine, B.N., de Beaulieu, J.-L., 2015. The Last termination in the South Indian Ocean: a unique terrestrial record from Kerguelen Islands (49°S) situated within the Southern Hemisphere westerly belt. Quat. Sci. Rev. 122, 142–157. https://doi.org/10.1016/j.quascirev.2015.05.010.
Verfaillie, D., Charton, J., Schimmelpfennig, I., Stroebele, Z., Jomelli, V., Bétard, F., Favier, V., Cavero, J., Berthier, E., Goosse, H., Rinterknecht, V., Legentil, C., Charrassin, R., Aumaître, G., Bourlès, D.L., Keddadouche, K., 2021. Evolution of the Cook Ice Cap (Kerguelen Islands) between the last centuries and 2100 ce based on cosmogenic dating and glacio-climatic modelling. Antarct. Sci. 33 (3), 301–317. https://doi.org/10.1017/S0954102021000080.
Verfaillie, D., Favier, V., Dumont, M., Jomelli, V., Gilbert, A., Brunstein, D., Gallée, H., Rinterknecht, V., Menegoz, M., Frenot, Y., 2015. Recent glacier decline in the Kerguelen Islands (49°S, 69°E) derived from modeling, field observations, and satellite data. J. Geophys. Res.: Earth Surf. 120 (3), 637–654. https://doi.org/10.1002/2014JF003329.
Verfaillie, D., Pelletier, C., Goosse, H., Jourdain, N.C., Bull, C.Y.S., Dalaiden, Q., Favier, V., Fichefet, T., Wille, J.D., 2022. The circum-Antarctic ice-shelves respond to a more positive Southern Annular Mode with regionally varied melting. Commun. Earth Environ. 3 (1), 1. https://doi.org/10.1038/s43247-022-00458-x.
Villa-Martínez, R., Moreno, P.I., 2007. Pollen evidence for variations in the southern margin of the westerly winds in SW patagonia over the last 12,600 years. Quat. Res. 68 (3), 400–409. https://doi.org/10.1016/j.yqres.2007.07.003.
Wang, Z., Liu, H., Cao, Y., 2018. Choosing a suitable ε w-p by distinguishing the dominant plant sources in sediment records using a new Pta index and estimating the paleo-δD p spatial distribution in China. Org. Geochem. 121, 161–168. https://doi.org/10.1016/j.orggeochem.2018.01.002.
Xia, Z., Oppedal, L.T., Van Der Putten, N., Bakke, J., Yu, Z., 2020. Ecological response of a glacier-fed peatland to late Holocene climate and glacier changes on subantarctic South Georgia. Quat. Sci. Rev. 250, 106679. https://doi.org/10.1016/j.quascirev.2020.106679.
Young, S.B., Schofield, E.K., 1973. Pollen evidence for late Quaternary climate changes on kerguelen Islands. Nature 245 (5424), 311–312. https://doi.org/10.1038/245311a0.
Zhao, B., Russell, J.M., Tsai, V.C., Blaus, A., Parish, M.C., Liang, J., Wilk, A., Du, X., Bush, M.B., 2023. Evaluating global temperature calibrations for lacustrine branched GDGTs: seasonal variability, paleoclimate implications, and future directions. Quat. Sci. Rev. 310, 108124. https://doi.org/10.1016/j.quascirev.2023.108124.
Zhao, J., Tsai, V.C., Huang, Y., 2022. A nonlinear model for resolving the temperature bias of branched glycerol dialkyl glycerol tetraether (brGDGT) temperature proxies. Geochem. Cosmochim. Acta 327, 158–169. https://doi.org/10.1016/j.gca.2022.04.022.
Zwier, M., van der Bilt, W.G., de Stigter, H., Bjune, A.E., 2022. Pollen evidence of variations in Holocene climate and Southern Hemisphere Westerly wind strength on sub-Antarctic South Georgia. Holocene 32 (3), 147–158. https://doi.org/10.1177/09596836211060495.
Zwier, M., Van Der Bilt, W.G.M., Schneider, T., D'Andrea, W.J., Bakke, J., Van Der Putten, N., Bjune, A.E., 2024. Holocene changes in the position of the Southern Hemisphere Westerlies recorded by long-distance transport of pollen to the Kerguelen Islands. Quat. Sci. Rev. 330, 108595. https://doi.org/10.1016/j.quascirev.2024.108595.